



Khait, Anatoliy and Ma, Zhihua ORCID logoORCID: <https://orcid.org/0000-0002-2426-3038> (2021) On an eddy viscosity model for energetic deep-water surface gravity wave breaking. *Journal of Fluid Mechanics*, 929. ISSN 0022-1120

Downloaded from: <https://e-space.mmu.ac.uk/628621/>

Version: Published Version

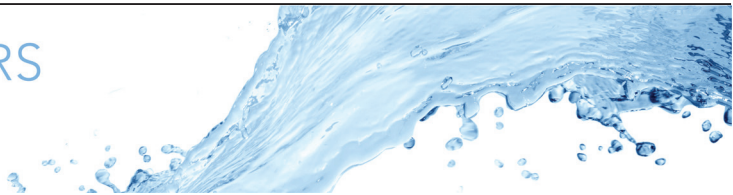
Publisher: Cambridge University Press (CUP)

DOI: <https://doi.org/10.1017/jfm.2021.863>

Usage rights: Creative Commons: Attribution 4.0

Please cite the published version

<https://e-space.mmu.ac.uk>



On an eddy viscosity model for energetic deep-water surface gravity wave breaking

Anatoliy Khait^{1,2,†} and Zhihua Ma^{1,†}

¹Centre for Mathematical Modelling and Flow Analysis, Department of Computing and Mathematics, Manchester Metropolitan University, Chester Street, Manchester M1 5GD, UK

²Department of Mechanical Engineering and Mechatronics, Faculty of Engineering, Ariel University, Ariel 40700, Israel

(Received 29 January 2021; revised 24 September 2021; accepted 27 September 2021)

We present an investigation of the fundamental physical processes involved in deep-water gravity wave breaking. Our motivation is to identify the underlying reason causing the deficiency of the eddy viscosity breaking model (EVBm) in predicting surface elevation for strongly nonlinear waves. Owing to the limitation of experimental methods in the provision of high-resolution flow information, we propose a numerical methodology by developing an EVBM enclosed standalone fully nonlinear quasi-potential (FNP) flow model and a coupled FNP plus Navier–Stokes flow model. The numerical models were firstly verified with a wave train subject to modulational instability, then used to simulate a series of broad-banded focusing wave trains under non-, moderate- and strong-breaking conditions. A systematic analysis was carried out to investigate the discrepancies of numerical solutions produced by the two models in surface elevation and other important physical properties. It is found that EVBM predicts accurately the energy dissipated by breaking and the amplitude spectrum of free waves in terms of magnitude, but fails to capture accurately breaking induced phase shifting. The shift of phase grows with breaking intensity and is especially strong for high-wavenumber components. This is identified as a cause of the upshift of the wave dispersion relation, which increases the frequencies of large-wavenumber components. Such a variation drives large-wavenumber components to propagate at nearly the same speed, which is significantly higher than the linear dispersion levels. This suppresses the instant dispersive spreading of harmonics after the focal point, prolonging the lifespan of focused waves and expanding their propagation space.

Key words: surface gravity waves, wave breaking

[†] Email addresses for correspondence: haitanatoliy@gmail.com, z.ma@mmu.ac.uk

1. Introduction

Surface gravity wave breaking is a highly important and challenging topic in engineering and environmental science. Violent breaking waves can produce destructive loads causing severe damage to, and even complete failure/loss of, naval, coastal and marine structures including ships, breakwaters, seawalls and oil and gas platforms (Babanin 2011; Ma *et al.* 2014, 2016). More broadly, wave breaking plays a crucial role in the planetary-scale atmosphere–ocean system by enhancing the exchange of mass, momentum and heat across the air–sea interface, thus influencing the Earth’s climate and weather (Kiger & Duncan 2012; Veron 2015). Breaking is also a major mechanism to dissipate wave energy, preventing the endless growth of wind waves (Melville 1996). Breaking wave models, in particular the accurate estimate of energy dissipated through the process, constitute a key part of numerical ocean wave forecast, which is essential to the safety of maritime activities including, but not limited to, fishery, ship navigation and offshore construction and operation.

Despite the vast amount of theoretical, experimental and numerical work reported in the past, the fundamental mechanism of wave breaking has not been understood thoroughly yet due to its extraordinary complexity. Wave breaking is a multi-scale and multi-phase problem, which involves multiple orders of scales ranging from the large orbital motions induced by surface water waves to the small air bubbles entrained into water mass and spray ejected into the atmosphere. To fully resolve the transient flow features of breaking waves in numerical simulations, extremely fine meshes and small time steps are needed. However, this will place a prohibitive burden on computing resources, restricting the computational domain of high-fidelity numerical models to only several representative wavelengths for three-dimensional (3-D) problems (Iafrati 2009; Lubin & Glockner 2015; Deike, Pizzo & Melville 2017).

It is known that the onset of breaking and the post-breaking evolution of the wave field are dependent on the breaking crest formation process, which is usually highly nonlinear (Khait & Shemer 2018). The development of breaking wave crest involves significantly large temporal and spatial scales that cannot yet be efficiently handled by high-fidelity numerical models alone (De Vita, Verzicco & Iafrati 2018; Iafrati, De Vita & Verzicco 2019). To effectively deal with these large scales, it is necessary to use simplified models such as the potential model which assumes the flow to be inviscid and irrotational. Under such an approximation, the flow velocity can be calculated as the gradient of the potential function. Although the potential approximation allows a substantial simplification of the problem, it disregards the crucial physical effects such as fluid viscosity, flow vorticity and two-phase features for wave breaking problems. Empirical closures are thus needed to take into account these important effects in the evolution of wave field subject to breaking.

Chalikov & Sheinin (2005) noticed that the free surface close to an unstable crest became nearly vertical upon the inception of breaking, and high-wavenumber spectral harmonics, accompanied by the nonlinear flux of energy from low to high wavenumbers, were generated. Damping the high-wavenumber components of the spectrum and therefore dissipating the associated energy can help to stabilise the computation (Chalikov & Sheinin 2005; Chalikov & Babanin 2014). The damping process was actually accomplished by introducing empirical terms to the free-surface boundary conditions. Similar approaches can be found in the extended high-order spectral models of Ducroz *et al.* (2012, 2016). For spectral ocean forecasting models, the nonlinear evolution of waves is considered as an energy cascade that transfers energy between different frequency harmonics. It allows us to take into account the spectral energy dissipation due to breaking

by using observation-based empirical source terms to parametrise the reduction of spectral components (Babanin *et al.* 2011; Annenkov & Shrira 2018).

Although damping high-frequency spectral components is computationally efficient, this kind of method has inherent restrictions. One significant difficulty is that wave breaking cannot be adequately described in the Fourier space because it is strongly localised in the physical space. An alternative semi-empirical closure for wave breaking was proposed by Tian, Perlin & Choi (2010, 2012). This model contains only one empirical constant as opposed to numerous fitting parameters used in other breaking approximations. Therefore, it is preferable for studying breaking processes at large spatial and temporal scales. A number of researchers have demonstrated this model's accuracy and robustness in the prediction of energy flux reduction for spilling and plunging breakers (Tian *et al.* 2010, 2012; Seiffert, Ducrozet & Bonnefoy 2017; Seiffert & Ducrozet 2018; Hasan, Sriram & Selvam 2019; Craciunescu & Christou 2020). However, notable disagreements with experimental measurements in terms of the surface elevation for strongly nonlinear wave trains have also been reported in the literature (Tian *et al.* 2012; Seiffert & Ducrozet 2018). In a scenario of a wave impacting on a marine structure, such a deficiency in surface elevation prediction could hinder the accurate calculation of wave loadings, and consequently affect the structural safety and integrity adversely (Bullock *et al.* 2007; Kapsenberg 2011; Hu *et al.* 2017). The underlying reason causing the discrepancy between the eddy viscosity model and laboratory experiments remains unclear.

This requests further investigation to identify the actual cause by producing a series of realistic wave breaking scenarios and analysing a considerable amount of detailed flow data. However, state-of-the-art laboratory facilities, in particular measurement equipment, are still deficient in the provision of needed large amount of high-resolution spatial and temporal flow information. To circumvent these restrictions, a hybrid low- and high-fidelity numerical model is developed and applied in the present work. We coupled a boundary element method (BEM) based fully nonlinear quasi-potential (FNP) model with a volume-of-fluid (VOF) method based two-phase incompressible Navier–Stokes (NS) model to formulate the hybrid FNP–NS model. This new approach is used to deal with the generation, propagation and breaking of deep-water waves and their post-breaking evolution. The accuracy of the numerical model is carefully assessed through a breaking wave train subject to modulational instability. The computed results are compared against the laboratory measurements and other numerical solutions reported in the literature. The FNP–NS model is then used to simulate the evolution of six broad-banded wave trains under non-, moderate- and strong-breaking conditions. The standalone FNP model, incorporated with the eddy viscosity enclosure, is also applied to compute these wave trains. This allows us to perform a comprehensive comparative study of breaking waves with the standalone FNP model and the hybrid FNP–NS model to quantify the deviations in surface elevation, energy dissipation and other important physical properties. Close attention is paid to the phases of free waves, the dispersion relationship between wavenumber and frequency, the trajectory of wave trains and their height before, during and after focusing. Detailed analyses of these important properties are carried out to examine the fundamental physical processes involved in breaking. For simplicity, sometimes we just use ‘breaking’ to stand for surface gravity wave breaking in the paper.

The remainder of the paper is organised as follows. The numerical methodology is described in § 2 and carefully validated against wave flume experiments in § 3. A detailed analysis of the wave train evolution observed in numerical simulations is presented in §§ 4.1 and 4.2. The breaking-induced phase shifting phenomenon and variation of wave

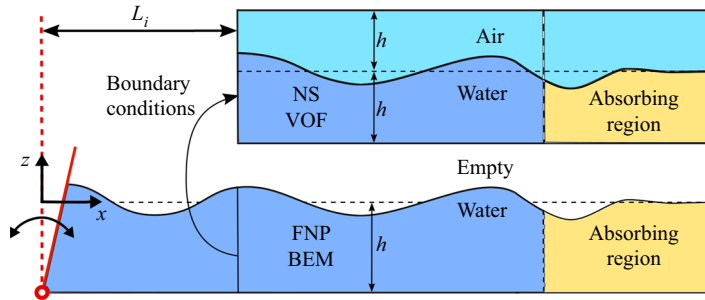


Figure 1. Schematic of the coupled FNP–NS model. BEM is used to discretise the FNP domain. The VOF method is used to discretise the NS domain. In the present work we also use ‘BEM’ and ‘VOF’ to refer to the low- and high-fidelity flow models, respectively.

train dispersion are discussed in §§ 4.3 and 4.4. Section 4.5 is devoted to the discussion of the suppression of dispersive defocusing and associated processes. Conclusions are drawn and practical implications are discussed in § 5.

2. Methodology

To reproduce realistically the generation, propagation and breaking of surface waves as well as their afterwards evolution, a number of numerical approaches are applied in the present work. This includes a FNP model and a two-phase incompressible NS model. A hybrid FNP–NS approach is developed by connecting the FNP and NS models through a one-way coupling strategy (see figure 1). Firstly waves are generated and propagated in the domain of the FNP model. The NS model is initialised after a certain amount of time when the waves arrive at its inlet boundary. Free-surface elevation and flow velocity computed by the FNP model at the coupling boundary are then transferred to the NS model (see more details in § 2.3).

As mentioned above, the FNP model is efficient for large-scale problems but ignores important physical effects. On the contrary, the NS model includes important physical effects and provides more detailed flow information at the cost of computational efficiency. The coupled FNP–NS model provides a way to balance low- and high-fidelity computations. Another benefit of using the coupled model is that it can produce more realistic scenarios without introducing artificial conditions for wave breaking (Lubin & Glockner 2015).

In the present work we focused on two-dimensional wave breaking problems. A series of numerical computations of breaking events under different wave conditions were carried out by using the standalone FNP model and the coupled FNP–NS model, respectively. Detailed descriptions of the FNP and NS models are given in the following.

2.1. The FNP model (BEM)

Under the potential approximation, the velocity field $\mathbf{U} = \{u, w\}$ is given by the gradient of the hydrodynamic potential φ , i.e. $\mathbf{U} = -\nabla\varphi$. The BEM is used to determine the distribution of φ across the FNP domain (Grilli, Skourup & Svendsen 1989; Grilli & Svendsen 1990). In this approach, the fluid flow is governed by Green’s second identity:

$$\alpha\varphi(r_s) = \oint_{\Gamma} \left(\frac{\partial\varphi}{\partial n}(r)\Phi(r, r_s) - \varphi(r)\frac{\partial\Phi}{\partial n}(r, r_s) \right) d\Gamma \quad (2.1)$$

Here, $\Phi(\mathbf{r}, \mathbf{r}_s) = -1/(2\pi) \ln |\mathbf{r} - \mathbf{r}_s|$ is the fundamental solution that represents the potential flow at point \mathbf{r} due to a source located at \mathbf{r}_s ; Γ is the closed boundary of the domain; $\alpha = \pi$ for regular nodes, and $\alpha = \pi/2$ for corner nodes; \mathbf{n} is the outward normal direction to Γ . The solution of (2.1) provides the value of $\partial\varphi/\partial n$ or φ at the point \mathbf{r} located on Γ . The third-order mid-interval interpolation (MII) technique (Grilli & Subramanya 1996) was used to discretise the boundary Γ for numerical solution of (2.1).

The free surface is subject to the dynamic and kinematic boundary conditions determining the time variation of its shape. Since we investigate strongly breaking wave field, the inclusion of empirical closures in the FNP model is required to stabilise the computation. For weakly damped waves (Ruvinsky, Feldstein & Freidman 1991), assuming the flow to be quasi-potential with small vortical velocity components, we can obtain the modified boundary conditions (Longuet-Higgins 1992; Dias, Dyachenko & Zakharov 2008; Dosaev, Troitskaya & Shrira 2021) given by

$$\frac{D\mathbf{r}}{Dt} = -\nabla\varphi - \underbrace{\nabla \times \Psi}_{\text{wave breaking}} \quad (2.2)$$

$$\frac{D\varphi}{Dt} = gz - \frac{1}{2}|\nabla\varphi|^2 - \underbrace{\tilde{p}_d \sqrt{gh} \frac{\partial\varphi}{\partial n} b_f(x)}_{\text{wave absorption}} + \underbrace{2v_{\text{eddy}} \frac{\partial^2\varphi}{\partial s^2}}_{\text{wave breaking}} \quad (2.3)$$

The vector streamfunction $\Psi = (0, 0, \psi)$ contains only a vortical part of the flow; g is the gravitational acceleration; h is the water depth; v_{eddy} is the closure constant for the wave breaking model; s is the direction tangential to the free surface. The value of the streamfunction at the free surface is governed by the vorticity equation. The exact form of this equation cannot be satisfied for potential flows, therefore its approximate version is used (Ruvinsky *et al.* 1991; Dosaev *et al.* 2021)

$$\frac{\partial}{\partial t} \frac{\partial\psi}{\partial s} = 2v_{\text{eddy}} \frac{\partial^2}{\partial s^2} \frac{\partial\varphi}{\partial n}, \quad (2.4)$$

where $\partial\varphi/\partial n$ is the solution of (2.1). Equation (2.3) is also responsible for wave absorption at the end of the domain, see figure 1. The dimensionless constant \tilde{p}_d characterises the strength of wave damping; function $b_f(x)$ determines the location of absorption region and the gradual increase of damping strength in the beginning of the region. The most effective absorption occurs when $\tilde{p}_d = 2$ (Khait & Shemer 2018, 2019b).

The no-penetration condition $\partial\varphi/\partial n = 0$ is applied at the bottom and right boundaries. A moving boundary with specified velocity is introduced at the left side of the domain to replicate the motion of a wave paddle, see figure 1. The domain size and grid resolution used in the simulations are summarised in table 1. Grid convergence study is presented in Appendix A. The integration time step was taken to satisfy the numerical stability criterion defined by the Courant number $CFL \leq 0.1$ (Grilli & Svendsen 1990).

Two approaches, namely regridding and empirical eddy viscosity, for approximating the energy dissipation due to wave breaking are considered in the paper. First, it was found that regridding the free-surface mesh at the instant of breaking inception can stabilise the numerical simulation without using the eddy viscosity closure, i.e. $v_{\text{eddy}} = 0$ in (2.2) and (2.3). For convenience, this model is designated as ‘BEMr’ in the following.

The grid nodes at the free surface represent the floating Lagrangian markers having all degrees of freedom. The distance between two neighbouring nodes is constantly

	Gaussian wave train	Modulated wave train
Length of the domain	$26\lambda_0$	$31\lambda_0$
Still water depth h	0.6 m	3.0 m
Length of the absorbing region		$7\lambda_0$
Free-surface grid resolution	30 nodes per λ_0	
Bottom boundary resolution	20 nodes per λ_0	

Table 1. Parameters of the BEM model. Details on the wave trains studied are presented in § 2.4; λ_0 is the carrier wavelength.

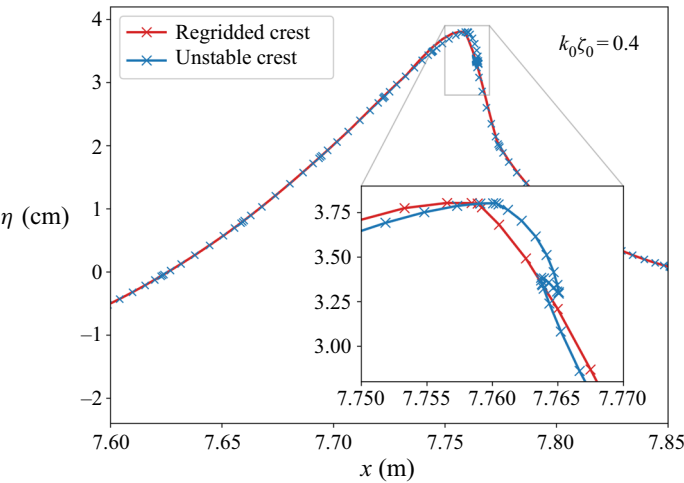


Figure 2. Shape of the pre-breaking wave crest before and after re-meshing. Cross markers show the mesh nodes on the free surface.

varying due to the propagation of nonlinear waves. The regridding method developed by Subramanya & Grilli (1994) establishes equal lengths of the arcs between all neighbour nodes as measured along the boundary elements. At the instance of breaking inception, the distance between the nodes at the pre-breaking crest becomes critically small leading to consequent crest overturning and loss of computation stability. The shape of the pre-breaking crest with and without regridding is shown in figure 2. It can be seen that the regridding method smooths the shape of the pre-breaking crest and removes the unstable overturning part.

A more advanced approximation for wave breaking energy dissipation is based on the eddy viscosity empirical closure suggested by Tian *et al.* (2010, 2012). According to this method, the location of breaking crest is established by using the geometrical criterion $S_b \geq S_c$; where S_b is the local free-surface slope, while its threshold value is $S_c = 0.95$. Once the location of breaking is determined, the eddy viscosity value is calculated by using the empirical relation (Tian *et al.* 2010, 2012)

$$v_{eddy} = \alpha \frac{H_b L_b}{T_b} \tag{2.5}$$

Here, H_b and L_b are the characteristic vertical and horizontal scales of a breaking event, respectively, while T_b is the characteristic time scale. All these values are determined by

Model type	BEMr	BEM _v
Eddy viscosity	$v_{eddy} = 0$	$v_{eddy} \neq 0$
Regridding	on	off

Table 2. Types of the breaking approximations.

using the empirical relations

$$\left. \begin{aligned} L_b &= \frac{24.3S_b - 1.5}{k_b} \\ T_b &= \frac{18.4S_b + 1.4}{\omega_b} \\ H_b &= \frac{0.87R_b - 0.3}{k_b} \end{aligned} \right\}. \quad (2.6)$$

Here, k_b and ω_b are local wave parameters; R_b is a geometrical factor showing the vertical asymmetry of breaking wave crest. The value of the proportionality constant in (2.5) is $\alpha = 0.02$. The determined eddy viscosity v_{eddy} is applied in the energy dissipation region with length L_b . The duration of eddy viscosity impact is T_b ; afterwards wave breaking is assumed to be finished implying $v_{eddy} = 0$. The methodology for determining all the required empirical constants is detailed in the work of Tian *et al.* (2012). Further, we designate the given eddy viscosity type of the BEM model as ‘BEM_v’, see table 2. In the following part of the paper, we use ‘BEM’ and ‘FNP’ interchangeably when referring to the potential flow model.

2.2. Two-phase NS model (VOF)

A VOF based two-phase incompressible NS flow solver namely *interFoam*, available in the open source library OpenFOAM, is used in the present work to develop a coupled FNP–NS model. The underlying NS model has been tested extensively for a series of wave–structure interaction problems including dam break, water entry, wave propagation and breaking wave impacting with fixed and moving structures, and the computed results have been verified against analytical solutions, laboratory experiments and other numerical results reported in the literature (Ma *et al.* 2016; Martínez Ferrer *et al.* 2016; Larsen, Fuhrman & Roenby 2019). The governing equations of the NS model represent momentum and mass conservation laws supplemented with the transport equation for the volumetric fraction of water phase

$$\frac{\partial \rho U}{\partial t} + \nabla \cdot (\rho U U) = \nabla \cdot (\mu \nabla U) + \sigma \kappa \nabla \alpha - \mathbf{g} \cdot \mathbf{r} \nabla \rho - p_d \quad (2.7)$$

$$\nabla \cdot U = 0 \quad (2.8)$$

$$\frac{\partial \beta}{\partial t} + \nabla \cdot (\beta U) = 0 \quad (2.9)$$

Density of the mixture ρ is determined by using the water volumetric fraction β as follows: $\rho = \beta \rho_w + (1 - \beta) \rho_a$, where ρ_w and ρ_a are the densities of water and air, respectively. Similar expression is used to determine the dynamic viscosity of the mixture μ .

	Gaussian wave train	Modulated wave train
Coordinate of the left boundary L_i	3.0 m	30 m
Length of the domain	$24\lambda_0$	$16\lambda_0$
Total height of the domain ($2h$)		1.2 m
Length of the absorbing region		$8\lambda_0$
Grid resolution		256 cells per λ_0

Table 3. Parameters of the VOF model. Details on the wave trains studied are presented in § 2.4; λ_0 is the carrier wavelength.

Equation (2.7) involves the dynamic pressure $p_d = p - \rho \mathbf{g} \cdot \mathbf{r}$, where \mathbf{r} is the radius vector in Cartesian coordinates and \mathbf{g} is the acceleration due to gravity. Surface tension is taken into account by the coefficient σ and the local interface curvature κ . The VOF based NS model (2.7)–(2.9) is discretised by a finite volume method on collocated grids and the transient flow problem is solved by the pressure-implicit with splitting of operators (PISO) method (Oliveira & Issa 2001). In the following part of the paper, we use ‘VOF’ and ‘NS’ interchangeably when referring to the two-phase incompressible viscous flow model.

To be consistent with the BEM model’s 2-D domain, the VOF domain was discretised by cuboid mesh cells with one single layer in the y direction, thus generating a pseudo-2-D domain, see figure 1. The left boundary of the VOF domain was displaced by L_i with respect to the BEM domain as shown in figure 1. The solution of the BEM model was thus used to determine both the initial and the left boundary condition for the VOF model to establish a one-way coupling between them. The numerical absorption of waves at the end of the domains was performed independently in both BEM and VOF models in order to avoid any interplay between them that may affect the wave train evolution process. The velocity field damping using effective viscosity was implemented near the far-end boundary of the VOF domain.

The Reynolds number for the wave trains considered in the research is (Iafrazi 2009)

$$Re = \frac{\rho_w g^{1/2} \lambda_0^{3/2}}{\mu_w} > 10^5. \tag{2.10}$$

It suggests that non-breaking wave trains may produce turbulence, as demonstrated by Babanin & Chalikov (2012). Even for a 2-D problem, the numerical simulation of flows at such high Reynolds number requires enormous computational effort to resolve all the scales involved in wave breaking. Assuming that the nearly laminar flow due to the surface gravity wave is dominant in the problems considered, it is expected to have the grid convergence in terms of free-surface elevation. In the course of the study it was established that the grid resolution of 256 cells per carrier wavelength (λ_0) is sufficient to produce converged solutions while balancing the computational efficiency and the capability to resolve key flow features. The details on grid independence are given in Appendix A, while the domain configuration is summarised in table 3.

The spatial and temporal numerical schemes for solution of the equations (2.7)–(2.9) were selected by following the recommendations for the *interFoam* solver (Larsen *et al.* 2019). Adaptive time step was used and the stability criterion was set as $CFL \leq 0.65$.

2.3. Coupling of the FNP and NS models

The coupling of the FNP and NS models was achieved through the following steps. Firstly, the velocity field \mathbf{U} was constructed in the interior area of the BEM domain using the known boundary values of φ and $\partial\varphi/\partial n$. The values of \mathbf{U} in the BEM domain were calculated at the coordinates corresponding to the cell centres of the VOF mesh. Several numerical techniques of evaluation of $\mathbf{U} \equiv \{u, w\} = -\nabla\varphi$ were examined in terms of accuracy and computational efficiency. It was found that the simplest central differencing scheme provides a reasonable accuracy, while keeping the process computationally efficient

$$\left\{ \begin{array}{l} u = -\frac{\varphi(x_{cell} + \Delta x, z_{cell}) - \varphi(x_{cell} - \Delta x, z_{cell})}{2\Delta x}, \\ w = -\frac{\varphi(x_{cell}, z_{cell} + \Delta z) - \varphi(x_{cell}, z_{cell} - \Delta z)}{2\Delta z}, \end{array} \right\} \quad (2.11)$$

where x_{cell} and z_{cell} are coordinates of the mesh cells of the VOF domain. The resolution of the scheme $\Delta x = \Delta z$ was taken equal to 1/10 of the size of the VOF cell. Other resolutions, i.e. 1/6 and 1/16, were also tested. The values of the potentials $\varphi(x, z)$ in (2.11) were calculated in the BEM solver by selecting the location of the source at the coordinates $\mathbf{r}_s = (x, z)$ and performing integration of (2.1). Secondly, the BEM velocity field and the free-surface profile were used to derive the appropriate boundary and initial conditions for the VOF model.

2.4. Wave train generation

Two types of wave trains are considered in this study. To validate the proposed hybrid BEM–VOF model against the experiments of Tian *et al.* (2012) and Seiffert & Ducrozet (2018), we investigate the wave breaking appearing in a narrow-banded wave train subjected to modulational instability. The surface elevation at the wavemaker location is

$$\eta(t) = a_0 \cos(\omega_0 t) + b \cos\left(\omega_1 t - \frac{\pi}{4}\right) + b \cos\left(\omega_2 t - \frac{\pi}{4}\right), \quad (2.12)$$

where a_0 and ω_0 are the amplitude and angular frequency of the carrier wave; frequencies of the sideband perturbations are $\omega_1 = \omega_0 - \Delta\omega/2$ and $\omega_2 = \omega_0 + \Delta\omega/2$. The following parameters were adopted from the case MI0719 of Seiffert & Ducrozet (2018) study: $\omega_0 = 4.398 \text{ s}^{-1}$, $\Delta\omega = 0.317$, $b/a_0 = 0.5$. The carrier angular frequency is related to the corresponding wavenumber $k_0(\omega_0)$ by the linear dispersion relation

$$\omega^2 = \left(gk + \frac{\sigma}{\rho}k^3\right) \tanh(kh). \quad (2.13)$$

For the range of the wavenumbers considered in the paper, capillary effect is not significant so we set $\sigma = 0$. The initial steepness of the wave train was $k_0 a_0 = 0.19$.

A broad-banded Gaussian-shaped focusing wave train was selected for a further investigation of wave breaking phenomena. This wave train implies the spatial periodicity of the free-surface elevation if the domain is sufficiently long, which is critically required for the accurate post-processing of simulation results. The strongest wave breaking in this case is expected in the vicinity of the focus location whose coordinate relative to the wave-generating boundary in the BEM domain ($x = 0$) was selected as $x_f = 8.5 \text{ m}$. For this group of numerical experiments, the length of computational domain is $L \approx 26\lambda_0 \approx 18 \text{ m}$. The coordinate $x_f = 8.5 \text{ m}$ is selected approximately in the centre of the domain so

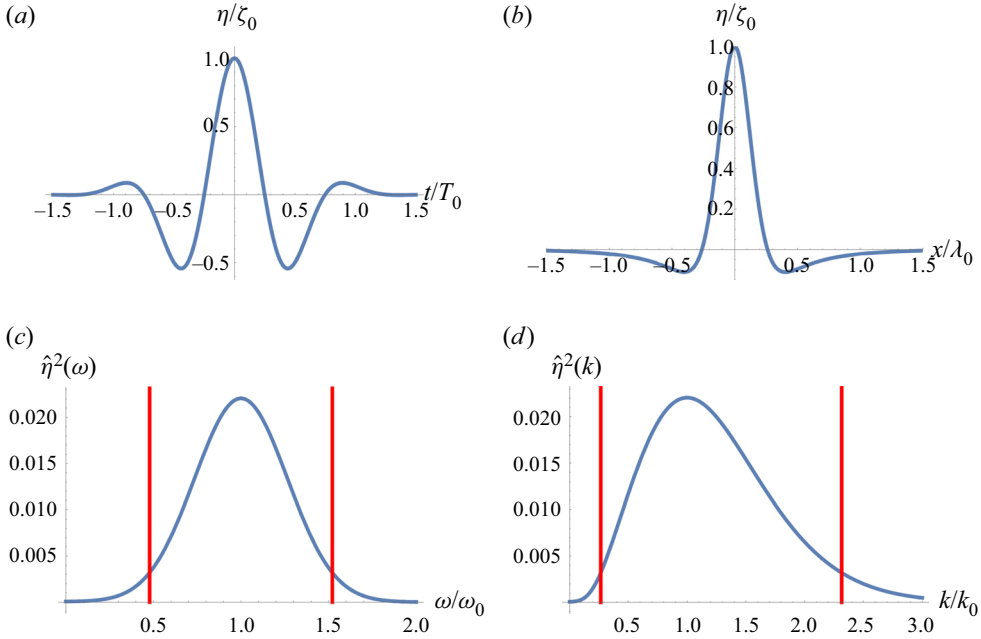


Figure 3. Broad-banded Gaussian-shaped focusing wave train considered in the study: (a) free-surface elevation at the focal point $x_f = 8.5$ m; (b) wave profile at the focal time $t_f = 0$; (c) frequency; and (d) wavenumber power spectra. Vertical red lines designate the range of frequencies and the wavenumbers containing 95 % of the spectral energy.

that it can provide enough space for wave train development in both pre- and post-breaking stages. The surface elevation variation with time at x_f is

$$\eta(t, x = x_f) = \zeta_0 \exp \left\{ - \left(\frac{t}{mT_0} \right)^2 \right\} \cos(\omega_0 t). \quad (2.14)$$

The parameter $m = 0.6$ determines the broad-banded wave train; the carrier wave period and angular frequency are $T_0 = 0.7$ s and $\omega_0 = 2\pi/T_0$, respectively. According to the linear dispersion relation (2.13) the carrier wavelength is $\lambda_0 = 2\pi/k_0 = 0.765$ m. The dimensionless water depth corresponds to deep-water conditions (Dean & Dalrymple 1991), i.e. $k_0 h = 4.93 > \pi$. The plot of $\eta(t)$ at the focal point x_f is shown in figure 3(a); the spatial surface elevation $\eta(x)$ at the instant of focusing t_f is plotted in figure 3(b).

In this study we investigate the evolution of free waves, and this requires us to exclude the bound waves from the BEM and VOF results. Since bound waves appear predominantly at high and low frequencies with respect to the carrier frequency ω_0 , it is possible to partially avoid their influence by band-pass filtering those regions. Consider the Fourier transform of surface elevation (2.14)

$$\hat{\eta}(\omega) = \mathcal{F}\{\eta(t)\} = \frac{\zeta_0}{2\sqrt{2}} m T_0 \exp \left\{ -\pi^2 m^2 \left(1 + \frac{\omega}{\omega_0} \right)^2 \right\} \left(1 + \exp \left\{ 4\pi^2 m^2 \frac{\omega}{\omega_0} \right\} \right). \quad (2.15)$$

The wavenumber spectrum for deep-water waves can be obtained by expressing ω from the linear dispersion relation (2.13) and substituting it into (2.15). The energy fraction δe

On an eddy viscosity breaking model

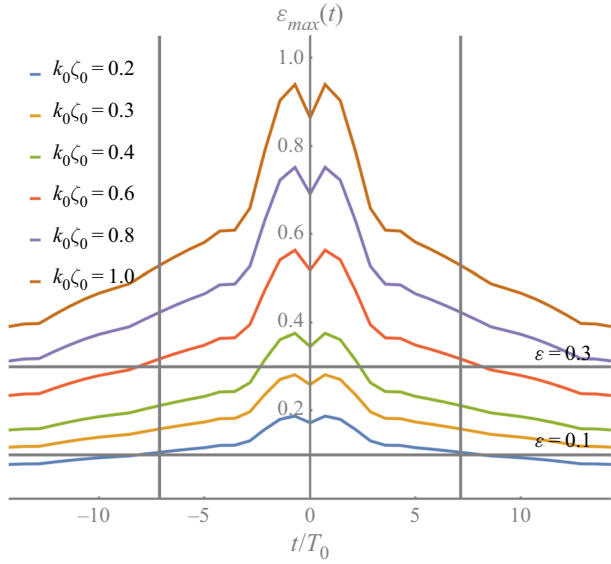


Figure 4. Time series of maximum wave train steepness (2.18) for all the considered cases. In this plot, the dispersive focusing appears at $t = 0$. Two grey vertical lines depict the range $-7.14 \leq t/T_0 \leq +7.14$ particularly considered in the study. Within this time interval the full length of the wave train is present in the limits of the computational domain of both BEM and VOF models.

contained in the frequency range $[\omega_0 - \Delta\omega, \omega_0 + \Delta\omega]$ is

$$\delta e = \frac{\int_{\omega_0 - \Delta\omega}^{\omega_0 + \Delta\omega} \hat{\eta}^2 d\omega}{\int_0^{+\infty} \hat{\eta}^2 d\omega} \approx 2\sqrt{2\pi m} \frac{\exp(-6\pi^2 m^2) (1 + \exp(4\pi^2 m^2))^2}{1 + \exp(2\pi^2 m^2)} \frac{\Delta\omega}{\omega_0}. \quad (2.16)$$

Solution of (2.16) with respect to $\Delta\omega$ assuming $\delta e = 0.95$ allows us to find the frequency band containing 95 % of the spectral energy. Following this procedure, the frequency and the wavenumber ranges that will be considered in the further analysis were estimated as follows: $0.48 \leq \omega/\omega_0 \leq 1.52$; $0.27 \leq k/k_0 \leq 2.31$. The power spectra with the corresponding frequency and the wavenumber bounds are depicted in figures 3(c) and 3(d).

Assuming deep-water dispersion $k = \omega^2/g$, the spatio-temporal variation of surface elevation can be obtained from (2.14) and (2.15) by using the linear approximation for water waves

$$\eta(x, t) = \mathcal{F}^{-1} \left\{ \hat{\eta}(\omega) \exp[ik(\omega)x] \right\} = \mathcal{F}^{-1} \left\{ \hat{\eta}(\omega) \exp \left[i \frac{\omega|\omega|}{g} x \right] \right\}, \quad (2.17)$$

where \mathcal{F}^{-1} is the inverse Fourier transform. At each instant t , the maximum steepness of the wave train is calculated as

$$\varepsilon_{\max}(t) = \max_{-\infty < x < +\infty} \left| \frac{\partial \eta(x, t)}{\partial x} \right|. \quad (2.18)$$

There exist a number of breaking inception criteria, including relatively simple geometric criteria and more complicated kinematic and dynamic principles (Perlin, Choi & Tian 2013). According to the simplest breaking onset criterion, a wave is expected to break if its steepness exceeds a certain threshold. In the current study we assume that a wave with steepness $\varepsilon > 0.3$ is likely to break. Increasing the wave steepness beyond this threshold may lead to a single or multiple breaking events. The strength of breaking is also dependent on the value of ε . Varying the value of the constant ζ_0 in (2.14), (2.15) and (2.17), six wave trains of different steepnesses $k_0\zeta_0 = 0.2, 0.3, 0.4, 0.6, 0.8$ and 1.0 are taken for investigation. Note that the spatial wave steepness ε is used throughout this work.

The time series of maximum wave steepness ε_{max} (2.18) for all the considered cases are plotted in figure 4. As expected for a broad banded focusing wave train, the peak value of ε_{max} is seen in the vicinity of the focal point, while it reduces farther away from this location. Note that in the course of the study, particular attention is given to the time interval $-7.14 \leq t/T_0 \leq +7.14$, when the full length of the wave train is present within the limits of the computational domain of both BEM and VOF models. The steepness of all wave trains within the given time interval is $\varepsilon_{max} > 0.1$, thus showing the significance of nonlinearities. A mild single breaking event may be expected for $k_0\zeta_0 = 0.3$, because the steepness satisfies the condition $\varepsilon_{max} > 0.3$ near the focal point for this case. If $k_0\zeta_0 \geq 0.6$, the steepness is greater than 0.3 within the entire time interval of interest as shown in the figure. This means that waves may continuously break throughout the evolution of the wave train.

Since the accuracy of wave generation is critical in the current investigation, the second-order accurate method for calculation of the wavemaker motion from the surface elevation was adopted (Khait & Shemer 2019b). The obtained wavemaker motion was then used to control the displacement of the wave-generating boundary in the BEM model, see figure 1. The surface elevation variation with time at the wavemaker location $\eta(x = 0, t)$ was calculated according to (2.17).

2.5. Spectrum decomposition

It is known that the domains of free and bound waves may overlap each other in both frequency and wavenumber spectra (Khait & Shemer 2019b). Despite limiting the analysis to a certain frequency range as discussed above, the effect of bound waves on the surface elevation spectrum may still be large, leading to complication of the analysis. To facilitate the study, the bound waves should be separated from the free waves by using Zakharov's weakly nonlinear theory for surface water waves (Zakharov 1968; Stiassnie & Shemer 1984, 1987; Krasitskii 1994). Within this theory, the surface elevation of nonlinear waves may be represented as a series of contributions appearing at different orders of small parameter ε : $\eta = \eta^{(1)} + \eta^{(2)} + O(\varepsilon^3)$; ε is the characteristic wave steepness conventionally defined in space; $\eta^{(1)}$ and $\eta^{(2)}$ are contributions of the free and the second-order bound waves, respectively.

Application of the discrete Fourier transform to the spatial distribution of free wave surface elevation $\eta^{(1)}$ gives the complex wavenumber spectrum $A(k_m)$, where k_m is the wavenumber of the m th harmonic. The free wave surface elevation is now

$$\eta^{(1)}(x) = \text{Re} \left\{ \sum_{m=0}^M A(k_m) e^{ik_mx} \right\}, \quad (2.19)$$

where M is the number of the discrete harmonics. Surface elevation of the second-order bound wave is

$$\eta^{(2)}(x) = \operatorname{Re} \left\{ \sum_{m=0}^M \sum_{n=0}^M \left[B(k_m, k_n) \exp(i(k_m + k_n)x) + C(k_m, k_n) \exp(i(-k_m + k_n)x) + D(k_m, k_n) \exp(i(-k_m - k_n)x) \right] \right\}. \quad (2.20)$$

The complex amplitudes $B(k_m, k_n)$, $C(k_m, k_n)$ and $D(k_m, k_n)$ are expressed in terms of $A(k_m)$, as given in [Appendix B](#).

At each instant t , the results of BEM and VOF simulations are processed to determine the distribution of surface elevation in space $\eta(x)$ as a series of discrete values at 2048 points equidistantly distributed along the domains. The range of the spatial coordinates considered in the analysis is $L_i \leq x \leq L_b$, where L_i corresponds to the inlet boundary of the VOF domain and L_b is the coordinate of the beginning of the absorbing region, see [figure 1](#). To decompose the fully nonlinear surface elevation $\eta(x)$ into free and bound waves it is assumed that $\eta(x) \approx \eta^{(1)}(x) + \eta^{(2)}(x)$. From this expression it is possible to find the complex spectra A , B , C and D iteratively by following the algorithm presented in Shemer, Goulitski & Kit (2007) and Khait & Shemer (2019a). In the first iteration, the free waves spectrum can be taken as $A(k) = \text{FFT}\{\eta(x)\}$, where FFT stands for the fast Fourier transform. Usually, 10 to 20 iterations are sufficient to converge the spectrum decomposition. Considering only the separated free waves spectrum $A(k)$ and limiting the analysis to the wavenumber range found in the preceding section, see [figure 3](#), it is possible to minimise the effect of bound waves.

3. Model validation and statement of the problem

Breaking in wave trains subject to the modulational instability (2.12) was investigated by Seiffert & Ducrozet (2018). The spatial evolution of waves was tracked in experiments by measuring the surface elevation at several coordinates along the wave flume. In particular, the emphasis was given to the following locations with respect to the wavemaker coordinate ($x = 0$): $x = 30.06$, 34.26 , 37.88 and 50.23 m; the total length of the wave flume is 148 m. They implemented the eddy viscosity approximation proposed by Tian *et al.* (2010, 2012) in a high-order spectral (HOS) code. To validate the BEM–VOF numerical model proposed in this paper, we compare our computations with the numerical and experimental results of Seiffert & Ducrozet (2018).

The computed and measured surface elevations are shown in [figure 5\(a–d\)](#). Note that spectrum decomposition is not applied here to separate the free and bound waves from the fully nonlinear wave train. Raw data of temporal elevation and spatial profile of the wave train are used for analysis. First, it can be seen that the BEM ν results agree very well with the HOS simulations of Seiffert & Ducrozet (2018). This confirms the validity of the BEM ν model. At the same time, the VOF solutions are very close to the experimental measurements and this demonstrates the accuracy of the two-phase high-fidelity model.

Now compare the results of BEM ν , BEMr and VOF simulations, see [figure 5\(e\)](#). It is clearly shown that at a distant location from the wavemaker, $WG14 = 50.23$ m, the plots of BEM ν and BEMr computations are close to each other. This suggests that the simple remeshing technique implemented in the BEMr model (Subramanya & Grilli 1994) can produce as good results as the complicated eddy viscosity approximation. It can be clearly

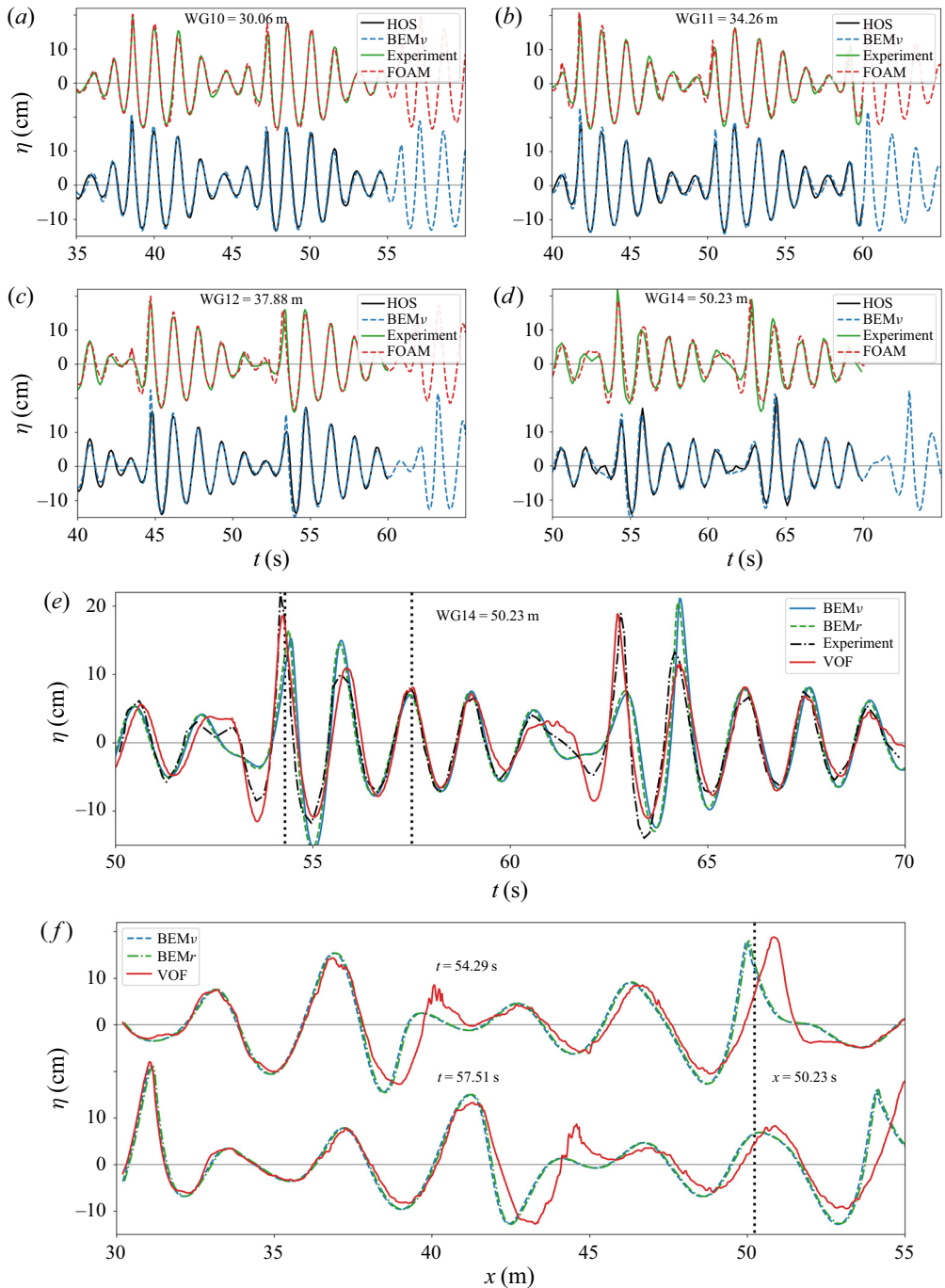


Figure 5. Measured and calculated surface elevations for a wave train subject to modulational instability at four wave gauges: WG10 = 30.06, WG11 = 34.26, WG12 = 37.88 and WG14 = 50.23 m (a–e). HOS simulations and experiments were performed by Seiffert & Ducrozet (2018). (f) Snapshots of free-surface profiles taken at two instants $t = 54.29$ and $t = 57.51$ s denoted by the vertical dotted lines in (e).

seen that there is a significant discrepancy between the low-fidelity calculations and the experiment from approximately 62.5 to 64.5 s regarding the peak elevations, potentially critical to maritime safety. A similar phenomenon can be observed for the time between 52 and 57 s. While the high-fidelity results are quite close to the measurements in terms of peak surface elevation. Similar observations were reported by Tian *et al.* (2012) and Seiffert & Ducrozet (2018). Seiffert & Ducrozet (2018) attempted to address this issue by modifying the eddy viscosity approximation without receiving much success. Figure 5(f) shows two snapshots of the spatial distribution of surface elevation obtained by the low- and high-fidelity models. These snapshots were taken at $t = 54.29$ and $t = 57.51$ s, two instants indicated by the two vertical dotted lines in (e). Note that there are no measurements of free-surface spatial profiles available in the literature for comparison here. Close to WG14 ($x = 50.23$ m), we can see that a very significant discrepancy between the numerical solutions appears in the vicinity of the steep wave crest at the moment $t = 54.29$ s. For a lower wave crest obtained at $t = 57.51$ s, the discrepancy is still quite visible though less significant than the moment $t = 54.29$ s.

The eddy viscosity approximation for wave breaking is based on the weakly damped wave theory (Ruvinsky *et al.* 1991; Longuet-Higgins 1992; Dias *et al.* 2008), which assumes the rotational components of the fluid velocity to be small. However, strongly breaking waves may generate significant non-potential flows; such as sheared currents, vortices, etc. (Iafrafi, Babanin & Onorato 2013; Deike *et al.* 2017; Lenain, Pizzo & Melville 2019). This could be a reason for the eddy viscosity method producing inaccurate prediction of surface elevation. To further our study of the eddy viscosity model and the underlying wave breaking physics, it is necessary to process free surface profiles by using the discrete Fourier transform. However, it is not trivial to carry out this task for the highly non-periodic wave profiles shown in figure 5(f). Therefore, we use a group of particularly designed Gaussian-shaped wave trains to facilitate the study in the following.

4. Results and discussion

4.1. Surface elevation

Here we investigate the evolution of Gaussian-shaped broad-banded wave trains (2.14) by using the standalone FNP model and the hybrid FNP–NS model. We selected a series of representative wave trains with steepnesses of $k_0\zeta_0 = 0.2, 0.3, 0.4, 0.6, 0.8$ and 1 . Computed surface elevations recorded at $x = 4.5$, $x = x_f = 8.5$ m (x_f is the expected focal point) and $x = 12.5$ m are plotted in figure 6. For wave trains with low steepness $k_0\zeta_0 \leq 0.4$, there is only one mild breaking event or even no breaking at all. Thus the eddy viscosity closure was not used for the cases illustrated in (a–c).

Figure 6(a) shows perfect coincidence of the results obtained by BEMr and VOF simulations when no breaking is present. It confirms the effectiveness of the BEM–VOF coupling used in the current study. The shape of the wave train at the focal point $x_f = 8.5$ m is very close to the linear prediction shown in figure 3(a). However, since the wave train is substantially nonlinear, a certain amount of asymmetry of the surface elevation before and after the focal point can be noticed. An increase in steepness, i.e. figures 6(b) and 6(c), leads to a significant deviation of either the BEMr solution or the VOF result from the linear estimation at the focal point, as expected for the steeper nonlinear waves. For the cases with higher steepness parameter $k_0\zeta_0 \geq 0.6$ shown in figure 6(d–f), both the BEMr and BEMv models were used. In compliance with the previous results, see § 3, no significant difference was noticed between the BEMr and BEMv results. Therefore, further analysis in the paper will be based on the BEMv model.

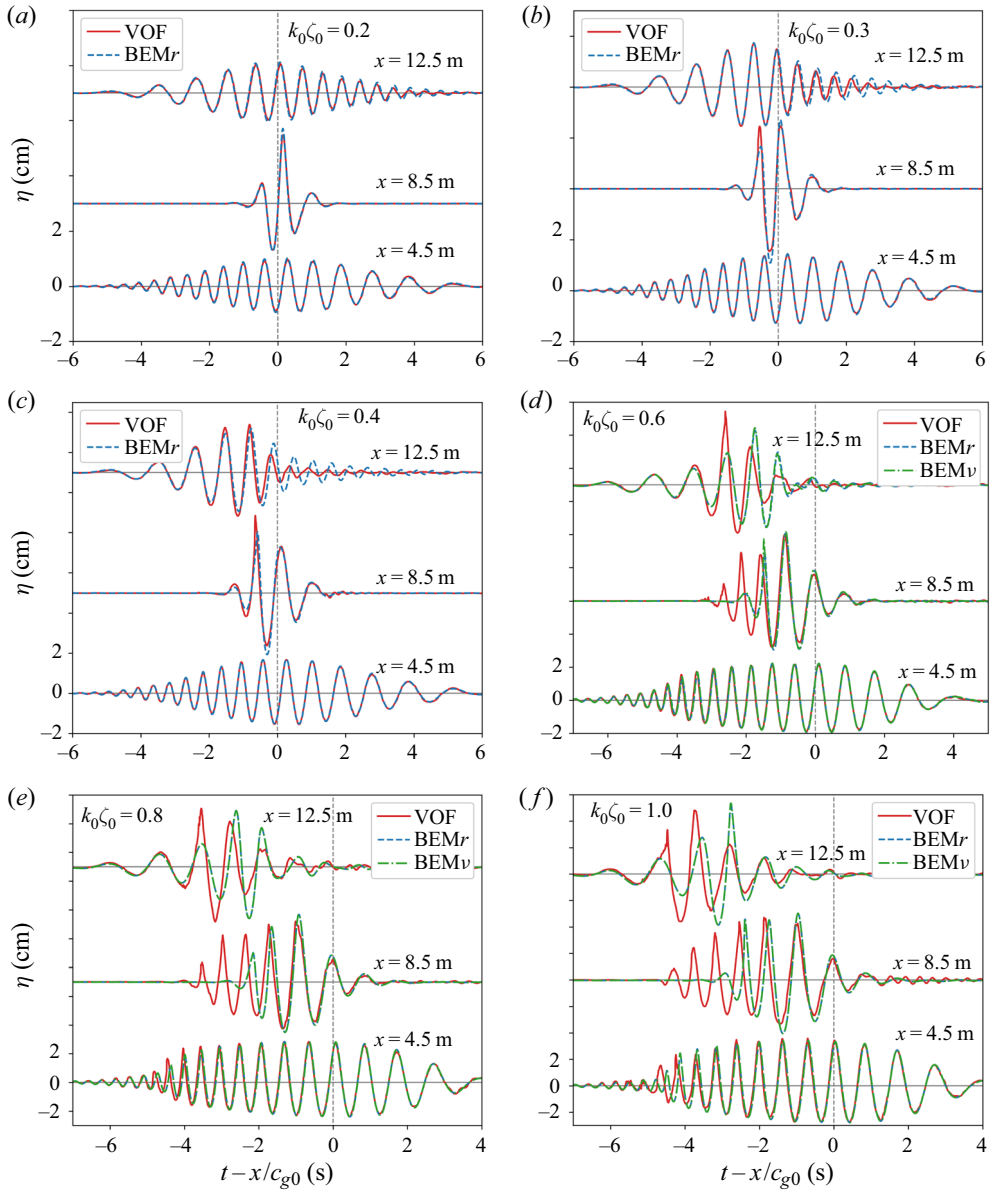


Figure 6. Surface elevation variation with time obtained by three numerical models: VOF, BEMr and BEMv. The value of time in the horizontal axes was displaced using the group velocity c_{g0} calculated for the carrier (peak) frequency of the wave train spectrum. The linear dispersive focusing is expected at $t - x/c_{g0} = 0$.

For wave trains with strong breaking shown in figure 6(d–f), the BEMv and VOF models produced quite similar results at $x = 4.5$ m. On the contrary, in the vicinity of and beyond the focal point, a considerable deviation between BEMv and VOF results is found and it increases with the steepness $k_0\zeta_0$. This indicates that certain physical processes associated with the breaking events are not accurately reflected by the quasi-potential eddy viscosity approximation in BEMv. It seems that this phenomenon is similar to the discrepancy we observed in § 3 for the experiments of Tian *et al.* (2012) and Seiffert & Ducrozet (2018).

Flooding contours of the velocity magnitude underneath the free surface are plotted in [figure 7](#) so that we can have a close look at the flow field to study the difference between the two-phase VOF solutions and the fully nonlinear potential BEM ν results. The fields are derived at $t = 35$ s near $x_f = 8.5$ m corresponding to the temporal and spatial location of the expected focal point according to the linear wave dispersion. The BEM ν model shows a quite smooth distribution of the velocity in the domain, contrary to the VOF solution, which embraces a certain perturbation component due to the vortical part of the flow. The plots show that the amplitude of the vortical velocity $-\nabla \times \Psi$ is no longer small as assumed in the weakly damped theory used by Tian *et al.* (2010, 2012). Consequently, the applicability of the eddy viscosity model for these problems is in question.

It is expected that the vortical flow consists of sheared currents and other local and distributed non-potential fluid motions (Iafrati *et al.* 2013; Deike *et al.* 2017; Lenain *et al.* 2019). For instance, several vortical structures are clearly shown in [figures 7\(b\)](#) and [7\(c\)](#). A more detailed investigation of the non-potential flows supposes the need of quantitative comparison of the BEM ν and VOF velocity fields. However, a meaningful comparison is practically impossible for the considered cases because the shapes of free surface obtained by these models are very different.

4.2. Energy dissipation due to wave breaking

The spatio-temporal evolution of the wave train calculated by the BEM ν model is illustrated in [figure 8](#) in terms of surface elevation. Wave breaking regions are highlighted in the figure as rectangular areas enclosed by black solid lines. The dimensions of these regions L_b in space and T_b in time were determined by the eddy viscosity closure (2.6). For each region the constant value of the eddy viscosity ν_{eddy} was calculated by using the formula (2.5). As expected, the non-breaking case, i.e. [figure 8\(a\)](#), does not have any predicted breaking locations. We also note that increasing the steepness $k_0\zeta_0$ can cause multiple breaking events instead of a single very strong one. This is because the wave train loses its stability much ahead of the focal point. At the same time, larger values of ν_{eddy} correspond to more energy dissipation.

The energy dissipation locations shown in [figure 8](#) do not overlap with each other. This means that in the studied wave trains, waves always break at different locations. Before the focal point, breaking always appears at the leading edge of the wave train because of the presence of short steep waves. On the contrary, after the focal point breaking locations move closer to the centre of wave train. Taking into account the fact that the leading edge of the wave train after the focal point consists of long waves, it can be assumed that those waves are more stable. This observation is usually involved in the spectral models of water waves, where the energy dissipation mostly at high frequencies is incorporated (Babanin *et al.* 2011; Annenkov & Shrira 2018).

Within the eddy viscosity quasi-potential approach, the energy dissipation process can probably be seen as a transformation of the energy associated with surface gravity waves into the rotational fluid flow energy. Since the considered broad-banded wave train occupies a restricted space, it is convenient to estimate the strength of wave breaking by tracing the amount of energy transferred by the wave train through different cross-sections, i.e. integral energy flux (Banner & Peirson 2007; Drazen, Melville & Lenain 2008; Tian, Perlín & Choi 2008; Derakhti & Kirby 2016). Taking into account that wave breaking is a strongly localised phenomenon, energy loss is associated with a particular location and appears as a reduction of the integral energy flux across the breaking location.

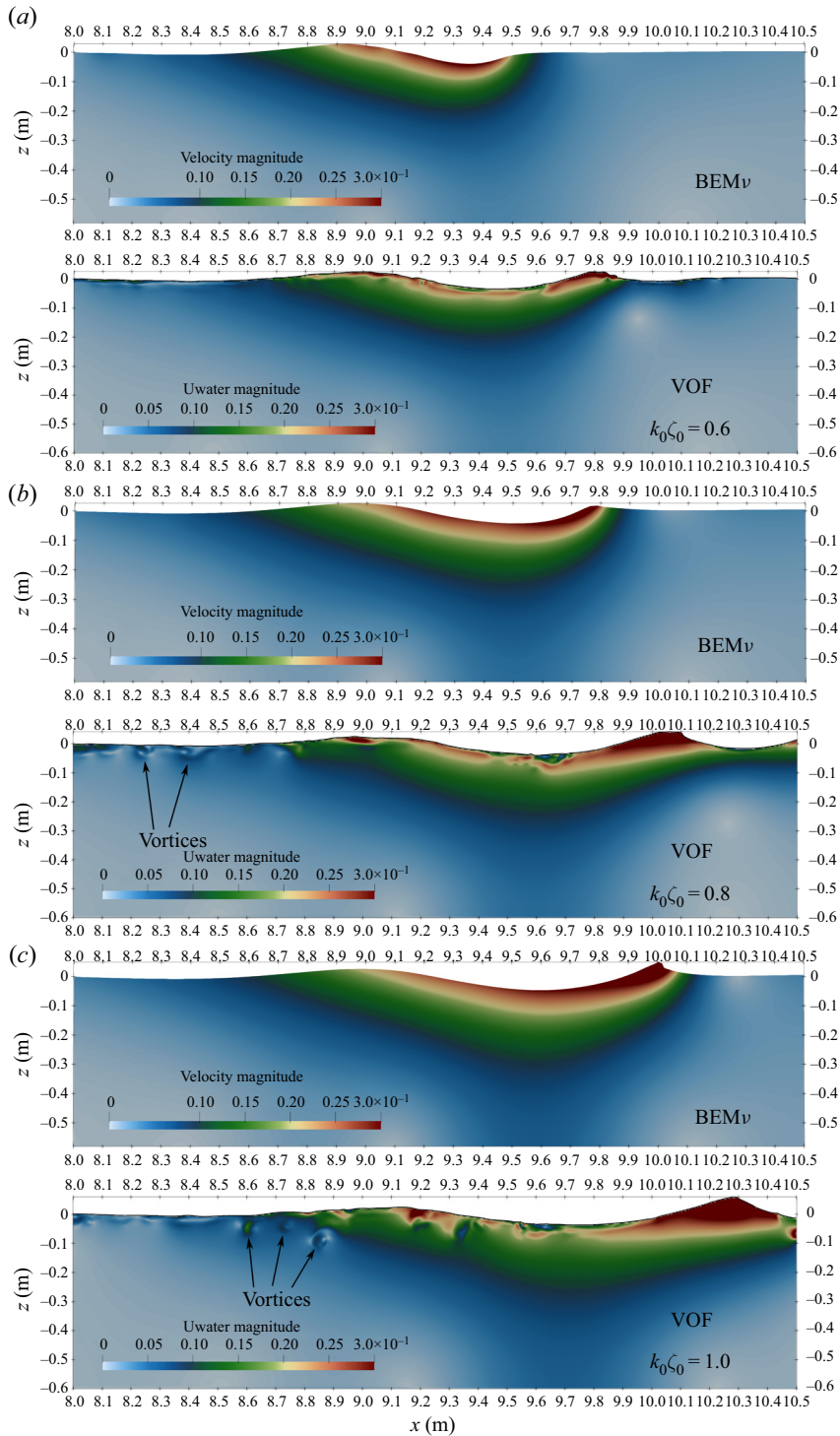


Figure 7. Distribution of the velocity magnitude $|U|$ beneath the free surface obtained in the BEM v and VOF models for three strongly breaking cases: (a) $k_0\zeta_0 = 0.6$, (b) $k_0\zeta_0 = 0.8$ and (c) $k_0\zeta_0 = 1.0$. The plots are obtained at the instant of focusing $t_f = 35$ s and in the vicinity of the focal point $x_f = 8.5$ m: the horizontal scale is $8 \leq x \leq 10.5$ m.

On an eddy viscosity breaking model

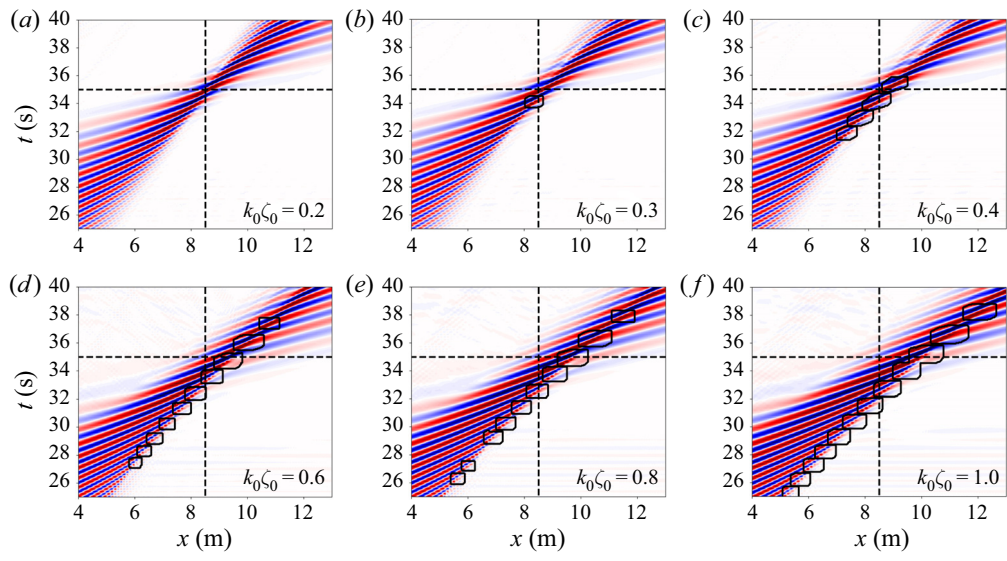


Figure 8. Energy dissipation regions predicted by the eddy viscosity approximation. (a–f) Present the wave trains having steepness parameter $k_0\zeta_0 = 0.2, 0.3, 0.4, 0.6, 0.8$, and 1.0 , respectively. The breaking regions are depicted by black solid lines. Colour shows the spatio-temporal variation of the surface elevation $\eta(x, t)$ calculated by the BEM ν model. Dashed lines show the location of the focal point expected according to the linear dispersion.

The total integral energy flux passing through the cross-section x in the VOF model is given by

$$F_{VOF}^{NL}(x) = \int_{-\infty}^{+\infty} dt \int_{-h}^{\eta(x,t)} \left\{ \frac{1}{2} \rho_w |U|^2 + \rho_w g z + p \right\} u \beta \, dz, \quad (4.1)$$

where $U = (u, w)$. This expression does not involve any physical simplification and thus determines the fully nonlinear value of the energy flux. In the VOF model, the volume fraction β is used to determine the percentage of water contained in a mesh cell. Thus the height of the water layer in each cell is βdz . The so-called dry and wet cells are distinguished by $\beta = 0$ and $\beta = 1$, respectively. Determination of the nonlinear energy flux in the BEM ν model is more complicated because the needed pressure p is not readily available in the solution. Simplification of (4.1) can be achieved by using the Bernoulli equation (2.3) and taking $U = -\nabla\varphi$

$$F_{BEM}^{NL}(x) = -\rho_w \int_{-\infty}^{+\infty} dt \int_{-h}^{\eta(x,t)} \frac{\partial \varphi}{\partial t} \frac{\partial \varphi}{\partial x} \, dz. \quad (4.2)$$

In laboratory it is not feasible yet to measure the nonlinear energy flux. Instead, a linearisation of (4.2) is usually applied (Banner & Peirson 2007; Drazen *et al.* 2008; Tian *et al.* 2008, 2010, 2012; Derakhti & Kirby 2016; Seiffert & Ducrozet 2018). Researchers usually assume the equipartition of total energy between the kinetic and potential parts, which is admissible for linear wave system. The linear approximation for the total energy density is $E = \rho_w g \overline{\eta^2}$, where the overbar represents averaging over the local wavelength. The linear approximation for the energy flux is then given by (Dean & Dalrymple 1991;

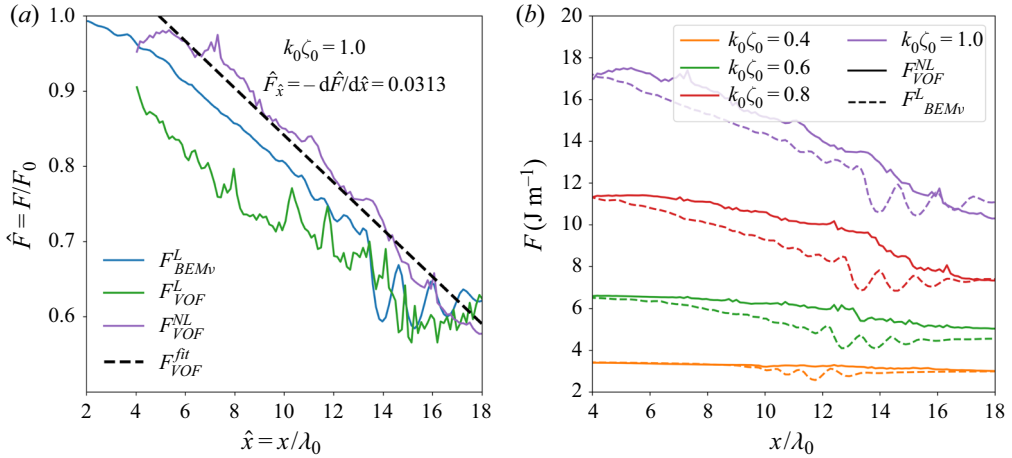


Figure 9. (a) Distribution of the dimensionless integral energy flux $\hat{F} = F/F_0$ along the computational domain $\hat{x} = x/\lambda_0$ for the wave train with the steepness parameter $k_0\zeta_0 = 1.0$. Black dashed line corresponds to the best fit of the nonlinear energy flux F_{VOF}^{NL} . (b) Dimensional integral energy flux computed for the wave trains of different steepness. Solid lines: VOF simulations (F_{VOF}^{NL}); dashed lines: BEMv simulations (F_{BEMv}^L).

Drazen *et al.* 2008; Derakhti & Kirby 2016)

$$F^L(x) = \int_{-\infty}^{+\infty} Ec_{gs} dt = \int_{-\infty}^{+\infty} \rho_w g c_{gs} \eta^2 dt. \quad (4.3)$$

Here, c_{gs} is the spectral-weighted group speed approximating the velocity of energy transferred by the given wave train

$$c_{gs} = \frac{\sum_j c_{g,j} a_j^2}{\sum_j a_j^2}, \quad (4.4)$$

where a_j and $c_{g,j}$ are the amplitude and the group velocity of the j th component of the wave packet spectrum.

The outcomes of (4.1) and (4.3) are compared in figure 9(a) for the steepest wave train with $k_0\zeta_0 = 1.0$. The dimensionless variables are introduced: energy flux $\hat{F} = F/F_0$ and spatial coordinate $\hat{x} = x/\lambda_0$; F_0 is the initial energy flux computed at $x \approx 0$. Figure 9(a) shows that the distributions of linear energy flux computed by the BEMv and VOF models, i.e. F_{BEMv}^L and F_{VOF}^L , somewhat deviate from each other. The nonlinear energy flux F_{VOF}^{NL} obtained by the VOF model provides the highest values of \hat{F} . In spite of the different trajectories of F_{BEMv}^L and F_{VOF}^{NL} , the bulk amount of energy dissipation computed by the VOF and BEMv models are close to each other for the cases considered here as shown in figure 9(b). This suggests that the eddy viscosity approximation used in the BEMv model predicts quite accurately the energy dissipation process, in agreement with earlier investigations (Tian *et al.* 2010, 2012; Seiffert & Ducrozet 2018; Hasan *et al.* 2019). It is interesting to note that the discrepancy in surface elevation calculation (see figure 6) does not significantly affect the amount of wave energy dissipated by breaking.

In the present work, we use the mean gradient of nonlinear energy flux $\hat{F}_{\hat{x}} = -d\hat{F}/d\hat{x}$ to characterise the strength of breaking. Such a quantify can be interpreted as the wave energy dissipation rate in space. For the VOF model, we produced the best fit of the energy flux

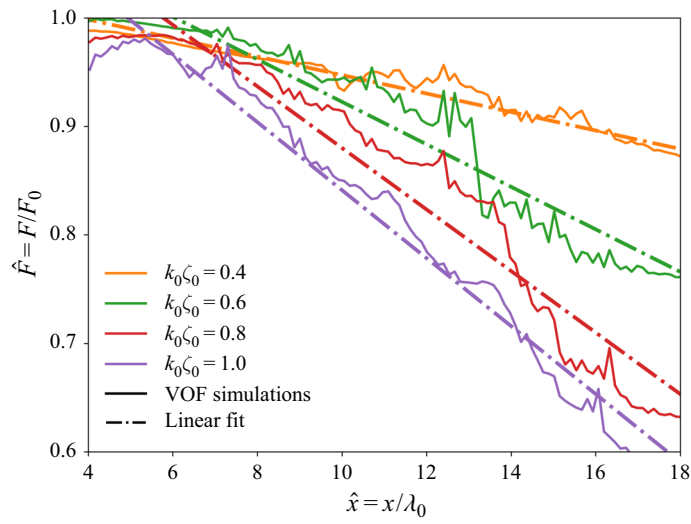


Figure 10. Distribution of the nonlinear energy flux F_{VOF}^{NL} obtained by the VOF model. The solid curves correspond to energy fluxes produced by the wave trains of different steepness $k_0\zeta_0$. The dash-dotted lines show the best fit of the data needed to compute the energy dissipation rate $\hat{F}_{\hat{x}}$.

$k_0\zeta_0$	$\hat{F}_{\hat{x}} = -d\hat{F}/d\hat{x}$	\tilde{U}/c_{g0}
0.3	0.00695	
0.4	0.00852	4.02×10^{-3}
0.6	0.0196	2.0×10^{-2}
0.8	0.0284	4.08×10^{-2}
1.0	0.0313	4.94×10^{-2}

Table 4. The values of the energy dissipation rate and the equivalent depth-uniform current computed for the wave trains of different steepness.

F_{VOF}^{fit} and illustrated it in figure 9(a) as the black dashed line, which has a gradient of 0.0313 in magnitude. The distributions of F_{VOF}^{NL} and F_{VOF}^{fit} for wave trains with different steepness $k_0\zeta_0$ are plotted in figure 10. The calculated values of $\hat{F}_{\hat{x}}$ are summarised in table 4. It can be seen from figure 10 and table 4 that the energy dissipation rate $\hat{F}_{\hat{x}}$ increases with the wave train steepness $k_0\zeta_0$.

Based on a scaling analysis, the breaking parameter b was used by Duncan (1983) and Drazen *et al.* (2008) to characterise energy dissipation caused by wave breaking. This parameter provides a quantitative relationship between the kinematics of breaking and the dynamics of energy loss. Importantly, the value of this parameter can be estimated from the field observations of whitecaps (Drazen *et al.* 2008). It can be instructive to quantify the value of the parameter b for the computations performed in the current study. This will also allow us to assess the genuineness of numerical models by comparing the calculated results against a set of published experimental and computational data.

According to Derakhti & Kirby (2016) the parameter b can be introduced by involving numerical results in the following way:

$$b\rho_w g^{-1} c_b^5 = \epsilon = \frac{\int_{x,t} \Delta F}{\tau_b}, \quad (4.5)$$

where ϵ is the averaged wave energy dissipation rate, ρ_w is the water density, c_b is the phase speed of the breaking crest, ΔF is the loss of the total wave energy flux according to (4.1) or (4.3). The time scale of active breaking is related to the period of breaking wave as $\tau_b = \alpha_t T_b$. According to Drazen *et al.* (2008), Kleiss & Melville (2010), and Derakhti & Kirby (2016), here, the proportionality constant is taken as $\alpha_t = 0.75$. The wavenumber k_b of a breaking wave is determined from the geometry of the breaking crest according to Tian *et al.* (2010, 2012) and Derakhti & Kirby (2016). Other parameters for the breaking crest are related to k_b as follows: $c_b = (g/k_b \tanh k_b h)^{1/2}$; $T_b = 2\pi/(k_b c_b)$. After substituting these into (4.5) we can obtain

$$b = \frac{g \int_{x,t} \Delta F}{\alpha_t \rho_w c_b^5 T_b}. \quad (4.6)$$

Since multiple breaking events are observed in our simulations, the averaged parameters of the breaking crest are used as shown in the expression (4.6). Note that the total energy flux losses obtained by the VOF and BEM ν models are very close to each other as shown in figure 9(b).

The calculated values of breaking parameter b (4.6) are compared with previously published results in figure 11(a). The widely used empirical parametrisation for b as a function of linear wave slope S is adopted from Romero, Melville & Kleiss (2012): $b = 0.4(S - 0.08)^{5/2}$. The wave slope S is the maximal wave steepness calculated for the linearly evolving wave train. For our cases one can estimate it as $S = k_0 \zeta_0$ (see figure 4). It is clearly illustrated in figure 11 that the values of b calculated in our study by both VOF and BEM ν models compare well with the empirical expression of Romero *et al.* (2012) and experimental data reported in the literature. Moreover, we present the result for a highly energetic breaking event under the condition $S > 0.8$, which has not yet been reported in the literature to the best of our knowledge. It is interesting to note that even for such strong wave energy dissipation, the parametrisation of Romero *et al.* (2012) is still applicable. Figure 11(b) suggests an exponential dependence of the breaking parameter b on the energy dissipation rate $\hat{F}_{\hat{x}}$. For the wave trains considered in the present study the following empirical expression can be suggested: $b = 3 \times 10^{-3} \exp(1.5 \times 10^2 \times \hat{F}_{\hat{x}})$.

4.3. Shift of phase due to wave breaking

In the beginning and at the end of computations only a part of the wave train is present within the domain. Therefore, in the analysis we focus on the interval $30 \leq t/T_0 \leq 56.8$, when the full length of the wave train is present within the domain. The surface elevation of free waves (2.19) obtained by the spectral decomposition (see § 2.5) of simulation results can be written as

$$\eta^{(1)}(x) = \sum_{m=0}^M |A(k_m)| \cos(k_m x + \xi_m), \quad (4.7)$$

where the phase is given by

$$\xi_m = \tan^{-1} \frac{\text{Im}\{A(k_m)\}}{\text{Re}\{A(k_m)\}}. \quad (4.8)$$

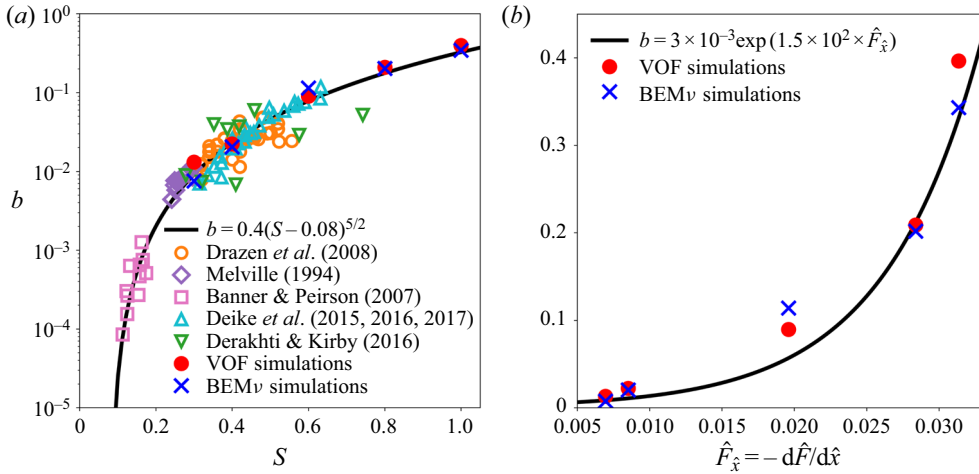


Figure 11. (a) Breaking parameter b as a function of the maximum wave steepness in the course of the linear wave train evolution, i.e. $S = k_0 \zeta_0$, see figure 4. Solid line: empirical expression based on scaling argument from Romero *et al.* (2012). The present simulations are in agreement with experimental and other reported numerical studies. The reference data are from the works of Melville (1994), Banner & Peirson (2007), Drazen *et al.* (2008), Derakhti & Kirby (2016) and Deike, Popinet & Melville (2015); Deike, Melville & Popinet (2016); Deike *et al.* (2017). (b) Breaking parameter b as a function of the energy dissipation rate $\hat{F}_{\hat{x}}$, see table 4.

It was found that the amplitude spectra obtained from the BEM ν and VOF simulations are practically identical in terms of the absolute value of the amplitude $|A(k_m, \omega_m)|$ regardless of wavenumber and angular frequency, cf. figure 12(a–d). This observation confirms the capability of the eddy viscosity approximation in predicting wave energy dissipation, which is in line with previous studies (Tian *et al.* 2010, 2012; Seiffert & Ducrozet 2018; Hasan *et al.* 2019), see also figure 9. Note that the energy contained in the spectrum is $\sum_{m=0}^M |A(k_m, \omega_m)|^2$. Therefore the visible divergence in surface elevation shown in figure 6 is very likely caused by the phase ξ_m . The phase difference between the VOF and BEM ν results relative to the carrier wave characteristics $\omega_0 T_0$ is given by

$$\frac{\Delta \xi_m}{\omega_0 T_0} = \frac{1}{2\pi} (\xi_{m,VOF} - \xi_{m,BEM\nu}). \quad (4.9)$$

The evolution of $\Delta \xi_m$ in time for different wavenumber k_m is plotted in figure 13 for the wave trains with steepness $k_0 \zeta_0 \geq 0.4$.

Figure 13 reveals a quite smooth and deterministic rather than stochastic evolution of the phase shift $\Delta \xi$ in time. Moreover, there is a strong dependence of $\Delta \xi$ on the wavenumber. The phase shift is relatively small at low wavenumbers, while at a high wavenumber it has a much pronounced growth with time. For instance, at the end of the wave breaking region the phase shift for a high wavenumber $k/k_0 \approx 1.5$ can increase by more than one full revolution, see figure 13(d). If the wave train steepness $k_0 \zeta_0$ and subsequently the energy dissipation rate $\hat{F}_{\hat{x}}$ are relatively low, the corresponding phase shift is much weaker, see figure 13(a). The phase difference between the BEM ν and VOF calculations could be due to the fact that the highly nonlinear rotational flows generated by breaking cannot be properly handled by the weakly potential eddy viscosity approximation.

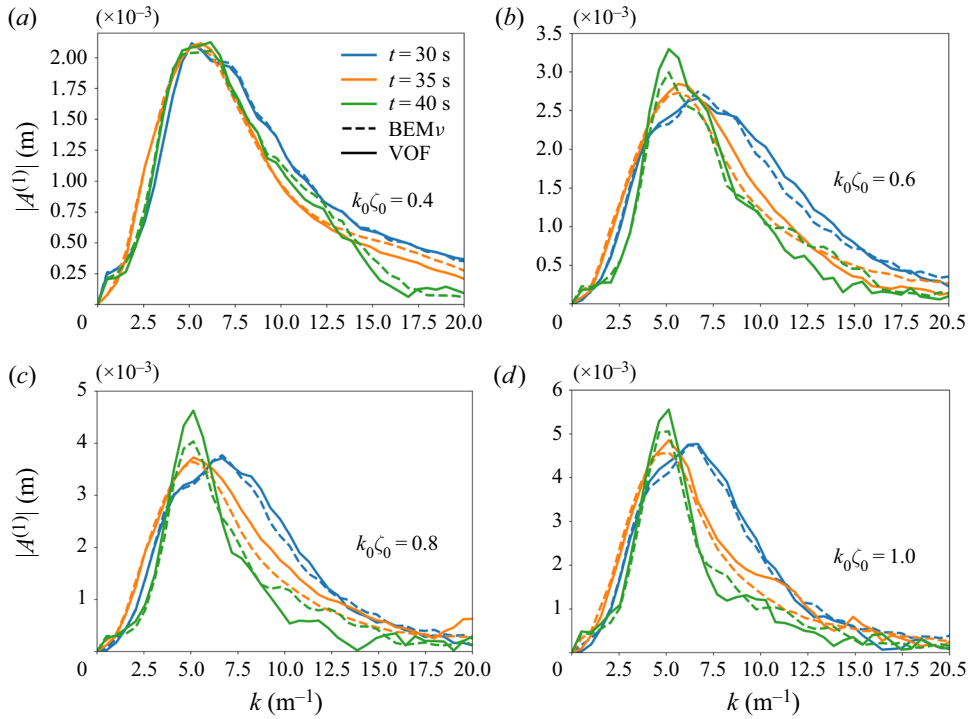


Figure 12. Free wave spectra obtained in VOF (solid lines) and BEMv (dashed lines) models. (a–d) Present the wave trains of different steepness parameter $k_0 \zeta_0$. Plots of different colour are obtained at various times of simulations.

Considering the dependence of phase shift on the wavenumber k and time t for the breaking strength $\hat{F}_{\hat{x}}$, we approximate it with the following expression:

$$\left. \frac{\Delta \xi}{\omega_0 T_0} \right|_{\hat{F}_{\hat{x}}} = \mathcal{E} \left[\frac{k}{k_0} \right]^{\Theta_K} \left[\frac{t}{T_0} \right]^{\Theta_T}. \quad (4.10)$$

The values of three coefficients \mathcal{E} , Θ_K and Θ_T change from one wave train to another due to different breaking strength. We applied the least squares method to obtain the dependencies $\mathcal{E}(\hat{F}_{\hat{x}})$, $\Theta_K(\hat{F}_{\hat{x}})$ and $\Theta_T(\hat{F}_{\hat{x}})$ from the numerical simulations, and present them in figure 14. It is shown that the rate of phase shift has a nonlinear dependence on time and wavenumber for relatively weak breaking; i.e. the values of the power coefficients $\Theta_K \approx \Theta_T \approx 4$ when $\hat{F}_{\hat{x}} < 0.01$. If breaking is strong, the dependence of phase shift on time tends to be linear with $\Theta_T \approx 1$, while the dependence on wavenumber is close to quadratic with $\Theta_K \approx 2$. Both Θ_K and Θ_T are reduced almost linearly with the increase of breaking strength $\hat{F}_{\hat{x}}$. In turn, the proportionality coefficient $\mathcal{E}(\hat{F}_{\hat{x}})$ demonstrates an exponential dependence on the energy dissipation rate $\hat{F}_{\hat{x}}$. Therefore it seems reasonable to infer from the analysis that the phase shift can become quite significant for strong-breaking events.

We applied the similar interpolation function to all the considered wave trains and obtained the corresponding phase shift in a dimensionless form

$$\frac{\Delta \xi}{\omega_0 T_0} = \mathcal{E} \left[\hat{F}_{\hat{x}} \right]^{\Theta_F} \left[\frac{k}{k_0} \right]^{\Theta_K} \left[\frac{t}{T_0} \right]^{\Theta_T}. \quad (4.11)$$

On an eddy viscosity breaking model

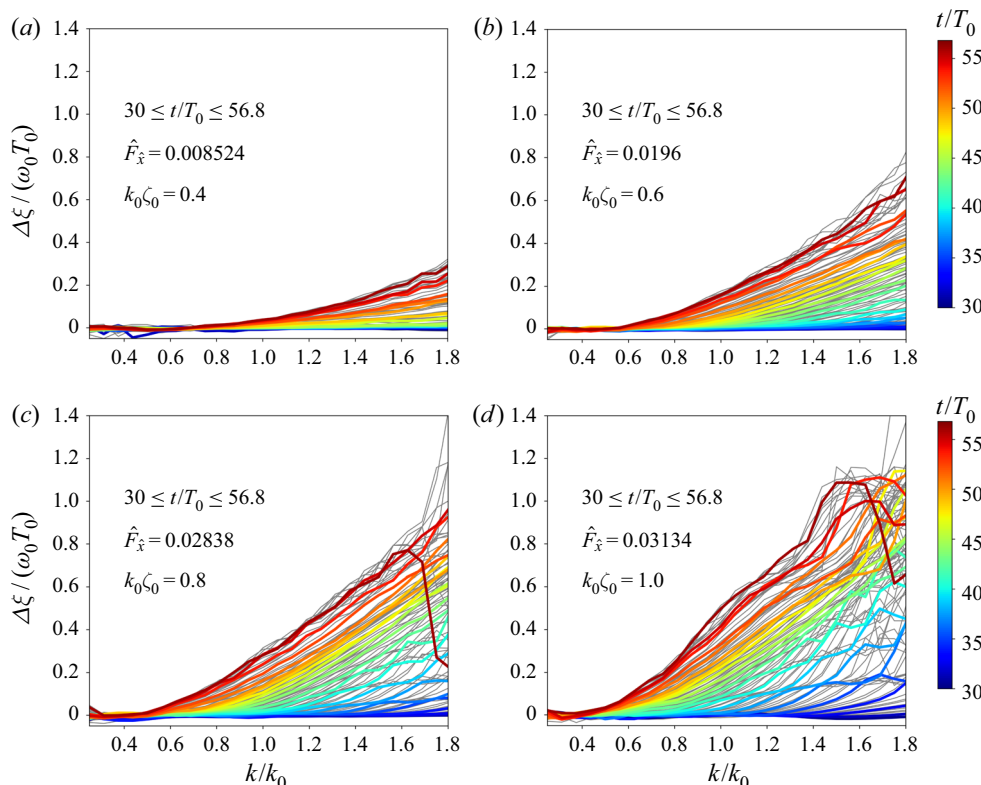


Figure 13. Evolution of difference in the free waves phases $\Delta\xi_m$ between VOF and BEMv simulations. The colour scheme from blue to red displays the plots obtained at different instances within the range $30 \leq t/T_0 \leq 56.8$. Grey plots show other not coloured data within the same time interval. (a–d) Correspond to the wave trains of various steepness $k_0 \zeta_0$.

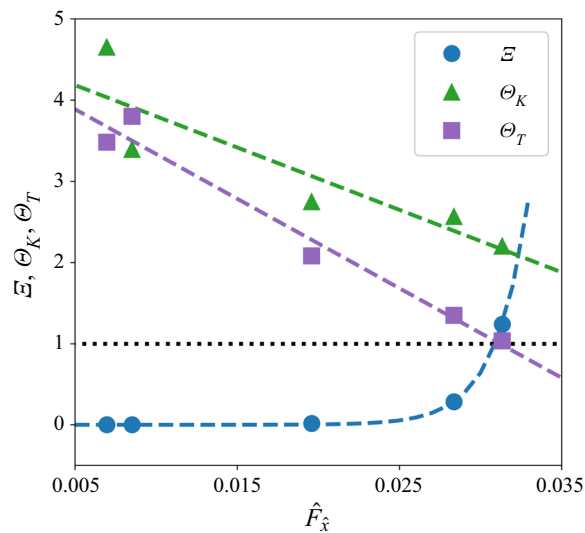


Figure 14. Dependence of the fitting coefficients Ξ , Θ_K and Θ_T (4.10) on the wave breaking strength $\hat{F}_{\hat{x}}$.

\mathcal{E}	Θ_F	Θ_K	Θ_T
5.02	1.926	2.362	1.2105

Table 5. Values of the dimensionless coefficients in the expression (4.11).

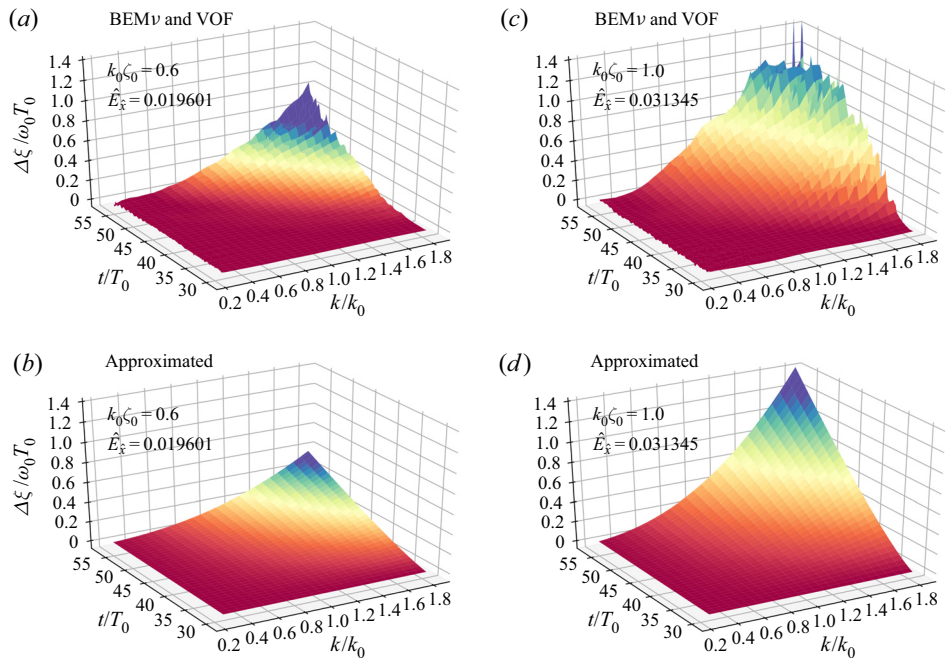


Figure 15. Phase shift $\Delta\xi/\omega_0T_0$ as a function of wavenumber and time obtained for the wave trains of different breaking strength: (a,b) $\hat{E}_x = 0.0196$; (c,d) $\hat{E}_x = 0.0313$. (a,c) Present the raw phase shift calculated using (4.9), while (b,d) are plotted using the interpolation (4.11).

Applying the least squares fitting of the numerical results, we obtained the coefficients and listed them in table 5. In addition to the previous findings, the value of $\Theta_F \approx 2$ implies a quadratic dependence of the phase shift on the energy dissipation rate.

In figure 15 the raw plots of $\Delta\xi(k, t)$ obtained from the numerical simulations are compared with those reconstructed from (4.11) in order to study the accuracy of the suggested approximation. It can be noticed that the plots obtained directly from the simulations using (4.9), see (a,c), exhibit fluctuations at high wavenumbers because the bound waves are not perfectly separated from the free waves by the decomposition method (§ 2.5). Even minor presence of unseparated bound waves significantly influences the phases of harmonics. Function (4.11) filters the fluctuations from the plots as presented in (b,d), while keeping a good qualitative and quantitative correspondence with the raw data extracted from the simulations.

The observed shift in phase is possibly related to the so-called phase-locking phenomenon reported by Derakhti & Kirby (2016). The phase-locking process is considered as a nonlinear linkage between high- and low-frequency wave components. This linkage was demonstrated by analysing the wavelet spectra of the surface elevation in the vicinity of the breaking event (Derakhti & Kirby 2016). The propagation velocity of

the high frequency components of the breaking wave was found to be different from that of the pre-breaking but stable wave.

4.4. Dispersion variation

It has been shown in various studies that the relationship between wavenumber and frequency may deviate from the linear dispersion relation (2.13) when the frequency spectrum is narrow. Krogstad & Trulsen (2010) studied the dynamic nonlinear evolution of unidirectional Gaussian wave packets using the nonlinear Schrödinger equation and its generalisations. It was observed that in the k - ω space the spectrum does not maintain a thin well-defined dispersion surface but develops into continuous distribution. The spectral components above and below the spectral peak were found to have the phase and group velocities close to that of the spectral peak. It was concluded that in some cases it is inappropriate to use the linear dispersion relation for the post-processing of experimental data.

Houtani *et al.* (2018a) and Houtani, Waseda & Tanizawa (2018b) have demonstrated that the dispersion characteristics of the Akhmediev breather solution to the nonlinear Schrödinger equation in deep water deviates significantly from the linear relationship (2.13). It was also shown that these findings extend beyond the applicability of nonlinear Schrödinger equation. Accordingly, the highly nonlinear non-breaking modulated wave trains also maintain the straight line relationship between the wavenumber and the instantaneous frequency; this line is tangent to the dispersion relation curve (2.13) at the carrier wavenumber. Gibson & Swan (2006) investigated the waves dispersion using the numerical simulations based on the third-order Zakharov equation. Inconsistency of the simulation results with the linear wave dispersion (2.13) was explained by analysing the third-order resonant interactions. The nonlinear energy transfer between harmonics in the free wave spectrum alters the values of the complex amplitudes. If interacting wave components are out of phase, this energy transfer will change the instantaneous phases of waves, which is reflected in the k - ω space. Adopting a similar Zakharov equation based theoretical model, the nonlinear correction to the dispersion relation for gravity waves in a constant depth was derived analytically by Stuhlmeier & Stiassnie (2019).

The phase of each free wave component is (Houtani *et al.* 2018a,b)

$$\xi(k, \omega, t) = kx - \omega t - \delta^{NL}(k, t), \quad (4.12)$$

where $\delta^{NL}(k, t)$ is the slowly varying nonlinear phase induced by the third-order resonant interaction between the waves (Gibson & Swan 2006). The angular frequency can be found from (4.12) by involving (2.13)

$$\omega(k) = -\frac{\partial \xi(k, \omega, t)}{\partial t} = \sqrt{gk \tanh(kh)} + \left\langle \frac{\partial \delta^{NL}(k, t)}{\partial t} \right\rangle. \quad (4.13)$$

When analysing a long time evolution of the wave group, the influence of $\langle \partial \delta^{NL} / \partial t \rangle \neq 0$ seen in k - ω spectrum may be interpreted as a deviation of the relationship $\omega(k)$ from (2.13).

In the current study it was found that the nonlinear contribution $\delta^{NL}(k, t)$ can be caused by the resonant interactions as well as the breaking-induced rotational flows. To construct the k - ω spectrum from BEMv and VOF computations the discrete distribution of the surface elevation in space is extracted from the numerical results. After applying spectrum decomposition (see § 2.5) the elevations of free waves at different instants are expressed

as a function $\eta(x, t)$. The discrete 2-D Fourier transform of this function in the k - ω space is given by

$$\hat{\eta}(k, \omega) = \frac{1}{NM} \sum_x \sum_t \eta(x, t) \exp(i(kx - \omega t)), \quad (4.14)$$

where N and M are the number of discrete values of η in x and t directions, respectively. Distributions of the absolute values $|\hat{\eta}(k, \omega)|$ obtained from the VOF simulations are shown in [figure 16](#).

The highest values of $|\hat{\eta}(k, \omega)|$ are located in a relatively narrow region approximately defining the dispersion relation $\omega(k)$. For the considered broad-banded Gaussian wave trains the distributions of $|\hat{\eta}(k, \omega)|$ have no visible deviation from the linear dispersion relation for both non-breaking and weakly breaking cases $k_0\zeta_0 = 0.3$ – 0.4 , cf. [figures 16\(a\)](#) and [16\(b\)](#). According to [figure 4](#), the maximum steepness of these wave trains is within the interval $0.2 < \varepsilon_{max} < 0.4$, indicating strong nonlinearity. Such dispersive properties are different from those discussed in Gibson & Swan (2006), Krogstad & Trulsen (2010) and Houtani *et al.* (2018a,b), where the linear dispersion relation was found to be inaccurate. The difference in the wave packet evolution may be related to: (i) the width of the spectra that is significantly higher for the wave trains considered in the current study, and (ii) the reduction of wave steepness and nonlinear effects away from the focusing location.

Subsequent increase of the wave train steepness, i.e. $k_0\zeta_0 > 0.4$, accompanied by the intensification of wave breaking leads to the deviation of the distribution of $|\hat{\eta}(k, \omega)|$ from the linear dispersion curve (2.13), cf. [figure 16\(c–e\)](#). The magnitude of this deviation is dependent on the wave train steepness parameter $k_0\zeta_0$. Note that the wave trains with $k_0\zeta_0 \geq 0.6$ are subject to breaking within the entire range of t and x used for computing the k - ω spectrum. Moreover, the deviation is observed only for the wavenumbers above the spectral peak k_0 , while long waves always follow the linear dispersion. To some extent, this phenomenon is correlated to the phase shift plotted in [figures 13](#) and [15](#), which is also present at high wavenumbers only.

The dependency of frequency on wavenumber $\omega(k)$ can be approximated from the distribution of $|\hat{\eta}(k, \omega)|$ by using the following weighting:

$$\omega(k_n) = \frac{\sum_m \omega_m |\hat{\eta}(k_n, \omega_m)|^2}{\sum_m |\hat{\eta}(k_n, \omega_m)|^2}. \quad (4.15)$$

The outcomes of applying such a weighting to the BEM ν and VOF simulations are plotted in [figure 16\(c–e\)](#) by dashed and dash-dotted lines. It is interesting to note that the dispersion curves of BEM ν and VOF are quite close to each other in (c), and both deviate from the linear dispersion curve. A further increase in breaking intensity, see (d,e), leads to a pronounced deviation of the VOF curve from the BEM ν one. This suggests that the nonlinearities in the potential wave fields are only partially responsible for the change of dispersion.

Approximate dispersion relations obtained from the BEM ν and VOF results based on (4.15) are plotted in [figure 17\(a\)](#) for the steepest wave packet $k_0\zeta_0 = 1.0$. It can be noticed that the weakly nonlinear dispersion relation (Melville 1983; Whitham 1999)

$$\frac{\omega^2}{gk \tanh kh} = 1 + \left(\frac{9 \tanh^4 kh - 10 \tanh^2 kh + 9}{8 \tanh^4 kh} \right) \varepsilon^2 \quad (4.16)$$

that takes into account the actual mean steepness of waves can largely explain the deviation of dispersion observed in the BEM ν model. In (4.16) we assume the steepness to be of

On an eddy viscosity breaking model

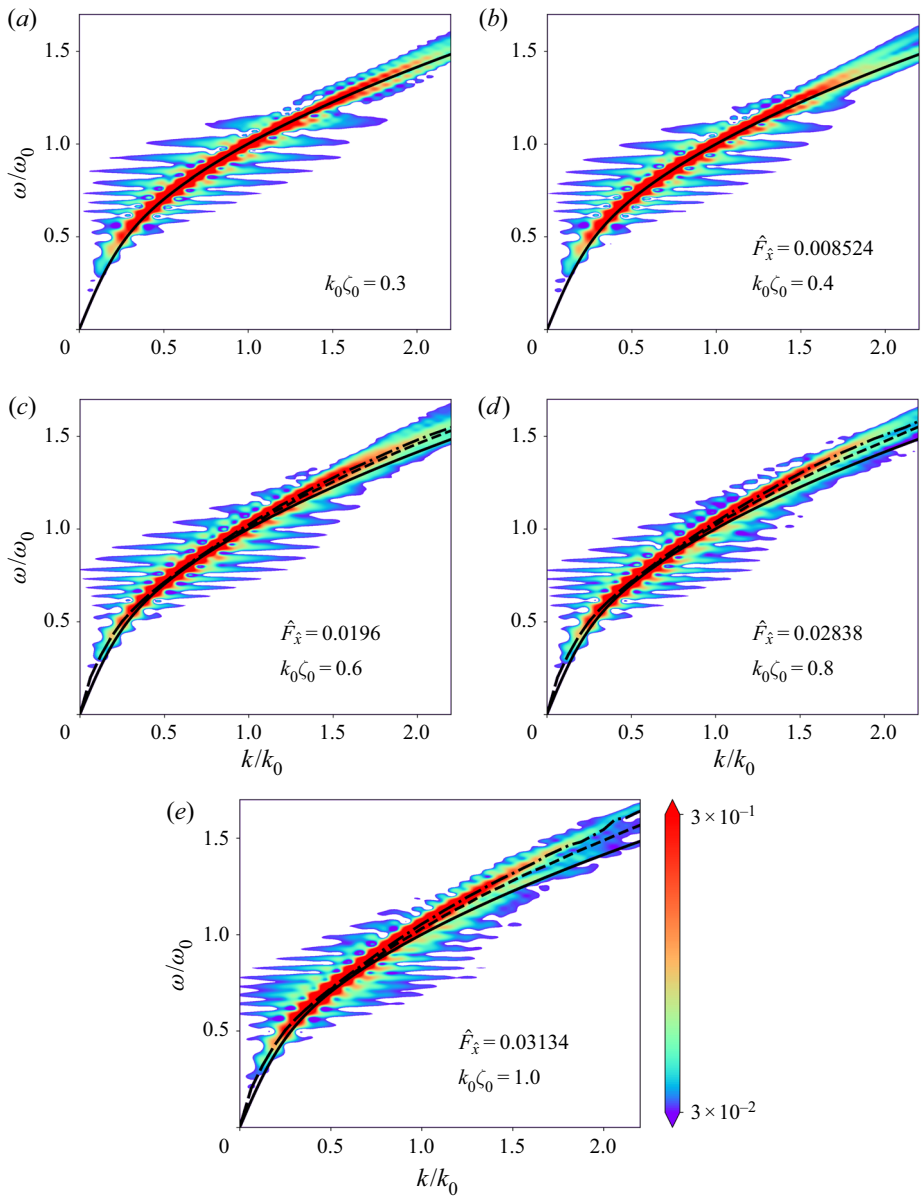


Figure 16. Dimensionless free wave k - ω spectrum $|\hat{\eta}(k, \omega)|/\max(|\hat{\eta}(k, \omega)|)$ obtained from the VOF simulations for wave packets with different steepness. A logarithmic colour scale is used. Solid line represents the linear dispersion curve (2.13) with capillary effects accounted for; dashed and dash-dotted lines show dispersion curves obtained by weighting (4.15) applied to BEMv and VOF computation results, respectively.

the order $\varepsilon \sim 0.3$ since the considered wave packet is constantly subject to breaking. This suggests that the effects observed in the BEMv model are probably caused by the nonlinear wave train evolution rather than the application of empirical eddy viscosity breaking approximation. See Appendix C for more discussion on this. To get further insights into the actual wave train dispersion observed in VOF computations, we attempt to correct the BEMv dispersion curve by involving the estimate of phase shift (4.11) and the

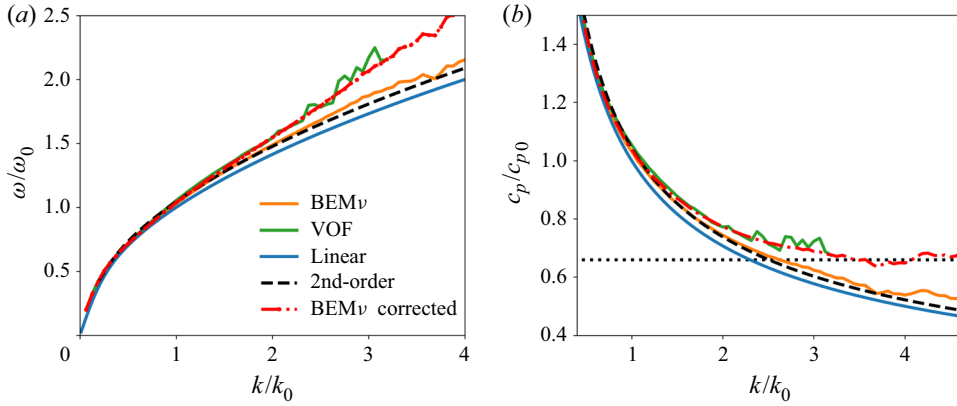


Figure 17. Dependence of (a) angular frequency and (b) phase speed on the wavenumber obtained from the results of BEM $_v$ and VOF simulations using (4.14) and (4.15). The correction to the BEM $_v$ curve is obtained by using (4.18). The steepest wave train is considered: $k_0\zeta_0 = 1.0$, $\hat{F}_{\hat{x}} = 0.03134$. The linear (2.13) and the weakly nonlinear (4.16) dispersion relations are given for reference.

expression (4.13)

$$\omega(k) = \omega_{BEM_v}(k) + \left\langle \frac{\partial \Delta \xi}{\partial t} \right\rangle \approx \omega_{BEM_v} \left\langle 1 + \Theta_T \Xi \left[\hat{F}_{\hat{x}} \right]^{\Theta_F} \left[\frac{k}{k_0} \right]^{\Theta_K} \left[\frac{t}{T_0} \right]^{\Theta_T - 1} \right\rangle. \quad (4.17)$$

Taking into account $(\Theta_T - 1) \sim 0$, the expression (4.17) can be simplified as

$$\omega(k) = \omega_{BEM_v} \left(1 + \Theta_T \Xi \left[\hat{F}_{\hat{x}} \right]^{\Theta_F} \left[\frac{k}{k_0} \right]^{\Theta_K} \right). \quad (4.18)$$

The corrected dispersion curve (4.18) for the BEM $_v$ model plotted in figure 17(a) is close to the VOF model. This suggests that the difference in wave dispersion between the two models is caused by the phase shift phenomenon discussed in § 4.3.

A similar observation regarding the satisfactory accuracy of (4.16) for steep non-breaking wave trains has previously been reported in the experimental study of Melville (1983), in which local phases were extracted from the surface elevation measurements by using the Hilbert transform. Nevertheless, Stansell & MacFarlane (2002) questioned the physical significance of phase reversal effect emphasised by Melville (1983) (reduction of the local phase speed below zero), as it can be subject to the peculiarity of Hilbert transform. On the other hand, Banner *et al.* (2014), Fedele, Chandre & Farazmand (2016) and Fedele, Banner & Barthelémy (2020) showed that the crest speed of a nearly breaking wave can significantly deviate from the phase speed suggested by both (2.13) and (4.16). The actual wave crest speed exhibits very fast variations: whether a crest experiences slowing down or speeding up depends on the dispersion regime it belongs to. Theoretical analyses demonstrated that quite complicated linear and nonlinear processes can be involved in this phenomenon. Though the present study is not aimed at addressing the complicated kinematics of breaking wave crests, it is of interest to analyse the dependence of phase speed on the wavenumber $c_p(k) = \omega/k$ evaluated from the dispersion relationships, see figure 17(b). Linear and BEM $_v$ dispersions show significant variation of the value of c_p within the considered range of the wavenumbers. On the other hand, the VOF data suggest a constant value of c_p at high wavenumbers. This implies

that relatively short waves propagate at a similar speed. Note that capillarity in (2.13) has an insignificant effect within the considered range of wavenumbers. Contrary to the observations of Houtani *et al.* (2018a,b), the property $c_p \neq c_p(k)$ is only held for high wavenumbers in the considered case.

Ramamonjiarisoa & Mollo-Christensen (1979) studied the dispersion anomalies of wind waves. They reported that the phase velocities for frequencies above the dominant wave are nearly constant and almost equivalent to the dominant wave's phase velocity. For mechanically generated narrow-banded wave trains, they noted the absence of such an effect except for a specific wave train subject to breaking. It is also found in their work that once the wave train starts to break, the harmonics above the carrier wave propagate at a very similar phase speed. Despite the experiments of Ramamonjiarisoa & Mollo-Christensen (1979) are based on narrow-banded wave trains, the observed effect they documented is possibly related to the phase shift phenomenon discussed in the current study. It is also important to note that Ramamonjiarisoa & Mollo-Christensen (1979) did not report/observe any deviation of the dispersion relation for nearly breaking wave trains. Therefore, rather than being induced by the nonlinearities of the potential wave field, the deviation of wave dispersion is more likely caused by the non-potential flows generated by wave breaking or wind.

We note that the expression (4.18) can be written in another form

$$\omega(k) = \omega_{BEMv} + k \times \tilde{U}. \quad (4.19)$$

Here, the empirical constant $\tilde{U} = \Theta_T \Xi \hat{F}_{\hat{x}}^{\Theta_F} \overline{c_{BEMv}}$ can probably be considered as the velocity of an equivalent depth-uniform current, which can trigger off the dispersion of waves similar to the phenomenon captured by the VOF model. Here, $\overline{c_{BEMv}}$ is the averaged characteristic phase velocity. The ratio \tilde{U}/c_{g0} calculated for each wave train ($k_0 \zeta_0 \geq 0.4$) is listed in table 4. Although the given expression does not necessarily reflect the actual currents generated by wave breaking, it provides us a tentative way to look at the underlying physics. This might be beneficial to the improvement of eddy viscosity model in the future.

4.5. Wave train trajectory

As demonstrated in § 4.4, wave breaking can cause high-frequency harmonics to propagate at a speed appreciably greater than that defined by the linear dispersion relation (2.13). Under these circumstances, short wave components propagate together with longer ones, thus preventing the dispersive spreading of wave packet. Such an evolution can lead to the distortion of wave train shape and spatio-temporal energy redistribution. Besides, the propagation speed of the entire wave packet can also be influenced by wave breaking nonlinearities. The propagation speed of wave packet energy in space is defined by the group velocity. Consider group velocity of the carrier (peak) frequency harmonic by differentiating (4.18)

$$c_{g0} = \left. \frac{\partial \omega}{\partial k} \right|_{k=k_0} \approx c_{g0, BEMv} \left(1 + \Theta_T \Xi \left[\hat{F}_{\hat{x}} \right]^{\Theta_F} \right). \quad (4.20)$$

The expression (4.20) suggests that the wave train propagation velocity increases with breaking intensity defined by the energy dissipation rate $\hat{F}_{\hat{x}}$. In this section, the dynamics of wave packet evolution is studied to verify these hypotheses.

The propagation velocity of a wave train can be evaluated by analysing the surface elevation envelope obtained from numerical simulations. At each instant t , the Hilbert

transform is applied to calculate wave train envelopes from free wave surface elevations $\eta(x, t)$ obtained by the BEMv and VOF models

$$\mathcal{H}(x) = \left| \eta(x) + \frac{i}{\pi} \text{PV} \int_{-\infty}^{+\infty} \frac{\eta(\chi)}{\chi - x} d\chi \right|, \quad (4.21)$$

and the dimensionless form is given by

$$\tilde{\mathcal{H}}(x, t) = \frac{\mathcal{H}(x, t)}{\max_{x,t} (\mathcal{H}(x, t))}. \quad (4.22)$$

In the limit of a linear system, the velocity of a Gaussian wave train is determined by the propagation speed of the envelope maximum. When waves become highly nonlinear, the instantaneous envelope is disturbed by the fast variations due to nonlinear interactions, which redistribute the energy $\tilde{\mathcal{H}}^2$ within the wave train. Since these variations do not determine the mean velocity of the energy propagation, the linear approach is not applicable. There is no strict method yet to determine the propagation speed of a strongly nonlinear wave packet. Following Pizzo & Melville (2016) here we define the wave train trajectory in the x - t space by tracing the motion of the centroid of the energy density

$$X_H(t) = \frac{\sum_x x \tilde{\mathcal{H}}^2(x, t)}{\sum_x \tilde{\mathcal{H}}^2(x, t)}, \quad (4.23)$$

where $X_H(t)$ is the instantaneous wave train coordinate. The instantaneous propagation speed of the wave train is then $v(t) = dX_H/dt$.

The distribution of $\tilde{\mathcal{H}}(x, t)$ obtained by the BEMv model is plotted in figure 18 for wave trains with different steepnesses. Note that the x coordinates are displaced by the linear focus location x_f and transformed using the linear group velocity of the wave packet. For the purpose of analysis, the range of x coordinates containing the dominant portion of the energy and determining the wave train boundaries is chosen by using the condition $\tilde{\mathcal{H}}^2 \geq 0.1$ as depicted by solid lines in figure 18. The distance between these boundaries can be used as a measure of instantaneous wave train length $L_H(t)$, see (e,f).

The spectrum of weakly nonlinear wave train varies slowly so that its shape is conserved within the time intervals considered in the study. The peak values and the spectral-weighted group velocities (4.4) are thus very close to each other, i.e. $c_{g0} \approx c_{gs}$. Consequently the value of c_{g0} gives a reasonable estimation of the wave packet propagation speed. Thus the wave train trajectory is aligned with the vertical axis as shown in figure 18(a), where the wave train has a low steepness $k_0\zeta_0 = 0.2$. The actual focal point for this case practically coincides with the linear prediction shown in the figure by dotted lines. Increasing the steepness to $k_0\zeta_0 \geq 0.3$ changes the free-surface elevation envelope. The wave train trajectory $X_H(t)$ (4.23) is plotted by the dashed lines in figure 18(c-f). It is shown that the intensification of wave breaking (growth of $k_0\zeta_0$ and $\hat{F}_{\hat{x}}$) leads to the inclination of wave train trajectory $X_H(t)$ from the vertical line, cf. (a-f). For the cases with relatively strong energy dissipation, i.e. $k_0\zeta_0 \geq 0.6$, the plots of $X_H(t)$ after the focal point are almost linear. This suggests that for each of these cases, breaking increases the wave packet propagation velocity $v(t) = dX_H/dt$ by a constant value equal to the gradient of the straight line.

The evolution of weakly nonlinear wave train, see figure 18(a), consists of two consecutive stages: (I) focusing within the time interval $t = 30$ –35 s, and (II) defocusing (dispersive spreading) within $t = 35$ –40 s. Breaking is only expected to occur in the

On an eddy viscosity breaking model

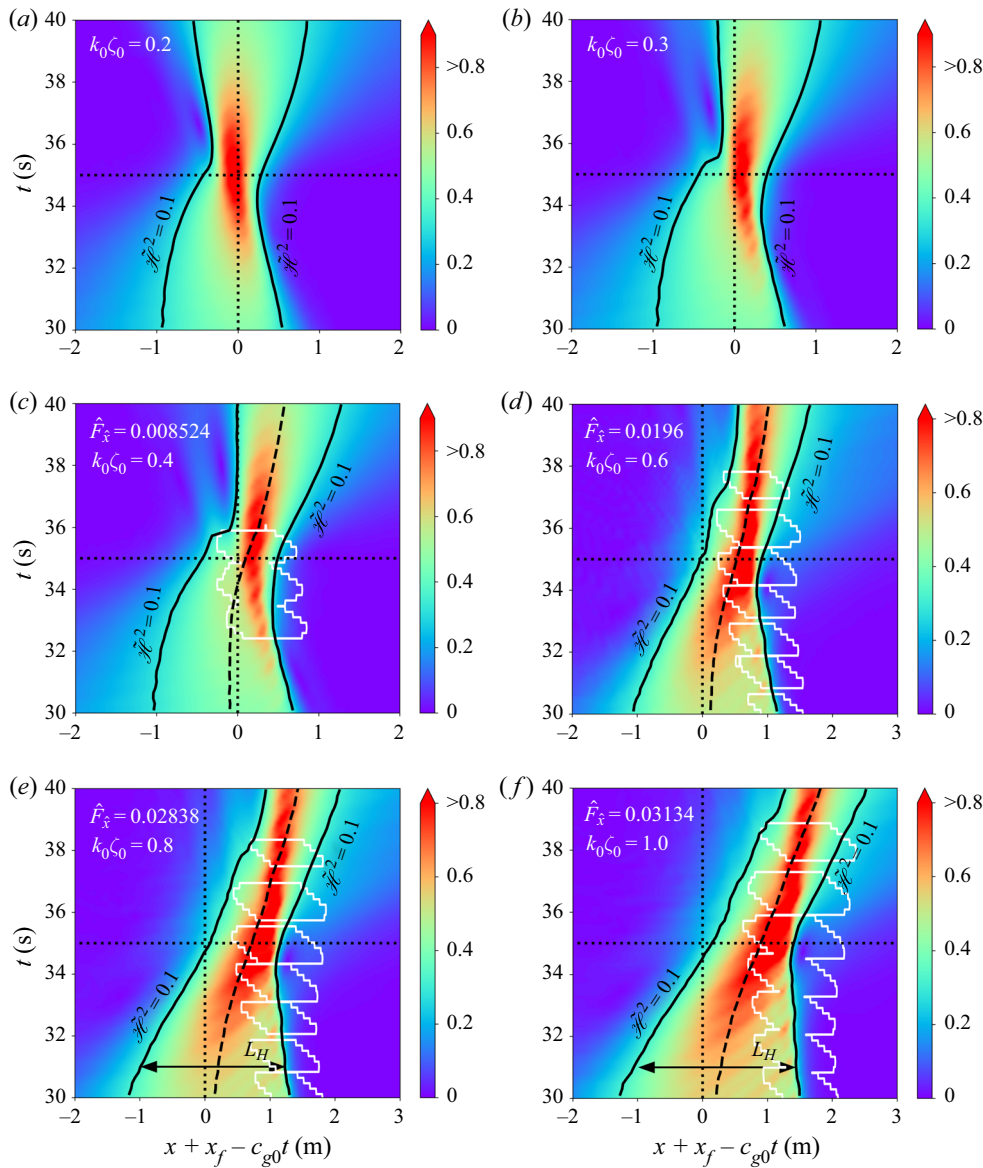


Figure 18. Surface elevation envelope $\mathcal{H}(x, t)$ (4.22) in x - t space obtained from the results of BEM ν computations: (a-f) present the wave trains of different steepness $k_0\zeta_0$. The colour scale has the range $0 \leq \mathcal{H} \leq 0.8$; higher values ($\mathcal{H} > 0.8$) are shown by red colour. The boundaries of the wave train corresponding to the energy level $\mathcal{H}^2 = 0.1$ are plotted by solid lines. Dotted lines depict the linear focal point location. The approximate wave train coordinates $X_H(t)$ (4.23) are plotted by dashed lines. The instantaneous wave train length $L_H(t)$ is indicated in (e, f). Areas of energy dissipation due to wave breaking predicted by the EVBM are indicated with white solid lines. Weak breaking events are disregarded in the plots by limiting values of eddy viscosity to $\nu_{eddy} > 10^{-4} \text{ m}^2 \text{ s}^{-1}$.

vicinity of the focal point at $t = 35$ s. Although the surface elevation envelopes of moderately nonlinear wave packets are distorted, both the focusing and defocusing stages are still clearly present, cf. figures 18(b) and 18(c). However, the occurrence of multiple stronger breakers modifies significantly the envelope evolution process for the cases with

high steepness $k_0\zeta_0 \geq 0.6$, for which a defocusing stage is no longer clearly visible in (d–f).

In view of similarity in the propagation regime of breaking wave trains, we consider the strongest energy dissipation case shown in figure 18(f). This wave train exhibits appreciable energy dissipation due to the strong and nearly continuous breaking within the full time range studied here, as clearly shown in figures 4 and 8. Despite this, the focusing stage is still largely pronounced. On the contrary, surprisingly, the spreading of wave train in the post-focusing stage is completely suppressed, see figure 18(f). Therefore, the reduction of wave height due to dispersion is less pronounced than in the low steepness cases presented in (a–c). This suggests that once extreme breaking waves appear, they propagate together without spreading until breaking dissipates the excessive energy and ceases. It also implies that such extreme waves could last longer than expected. Having a close look at the red areas shown in figure 18, where $\tilde{\mathcal{H}}(x, t) \geq 0.8$, we can clearly see their growth in time with wave train steepness especially for $k_0\zeta_0 \geq 0.6$. For low steepness wave trains $k_0\zeta_0 \leq 0.4$, the wave height reduces to less than 50 % of the maximum height by time $t = 38$ s. But for highly nonlinear waves $k_0\zeta_0 \geq 0.6$, the red regions can extend beyond $t = 40$ s. This means that increasingly intensified breaking can prolong the lifespan of extreme waves, and such an effect may not necessarily be trivial.

The surface elevation envelopes computed by the VOF model for non-breaking wave packets ($k_0\zeta_0 = 0.2$ and 0.3) coincide with the BEM ν results, cf. figures 18 and 19(a,b). The distributions of $\tilde{\mathcal{H}}(x, t)$ elicited from the VOF simulations for breaking wave trains with $k_0\zeta_0 \geq 0.4$ are presented in figure 19(c–f). Similar to the BEM ν computations, the evolution of non-breaking and weakly breaking wave trains consists of both dispersive focusing and defocusing stages, while there is no clear defocusing stage for strongly breaking cases in the domain of interest, cf. figures 18 and 19. At the same time, the wave train boundaries obtained by the VOF model become rough with the intensification of breaking.

The wave train trajectories $X_H(t)$ (4.23) obtained by the VOF model are plotted in figure 19 with dash-dotted lines. Corresponding plots of $X_H(t)$ taken for reference from figure 18 (BEM ν) are shown by dashed lines. In the focusing stage, the trajectories of weakly breaking wave trains computed by the BEM ν and VOF models are very close to each other as shown in figure 19(c). Once breaking is initiated in the vicinity of the focal point, see locations depicted by white solid lines in the figure, a small divergence of the trajectories appears. Note that such a deviation in trajectories is not seen prior to the first breaking event. For strong-breaking events as shown in figure 19(d–f), the divergence in wave trajectory between the VOF and BEM ν models becomes appreciably large. Wave trains computed by the VOF model propagate over longer distances and thus have higher propagation speeds compared with the BEM ν outcomes. These observations confirm our initial assumption that breaking can increase the propagation speed of wave trains compared with non-breaking scenarios. And this is associated with the phase shifting phenomenon as demonstrated in (4.20).

Applying linear regression to the trajectories $X_H(t)$ derived from BEM ν and VOF computations, the wave group propagation velocity $v(t) = dX_H/dt$ is estimated numerically and plotted in figure 20. The linear group velocity c_{g0} calculated by using the carrier frequency is included here for reference. Strongly nonlinear but non-breaking wave trains ($\hat{F}_{\hat{x}} \approx 0$) propagate at a speed moderately higher than the linear group velocity c_{g0} . The growth of propagation speed in this case is caused by the nonlinear resonant interaction between spectral harmonics. A similar outcome has been obtained analytically by Stuhlmeier & Stiassnie (2019) for nonlinear waves of Pierson–Moskowitz spectra.

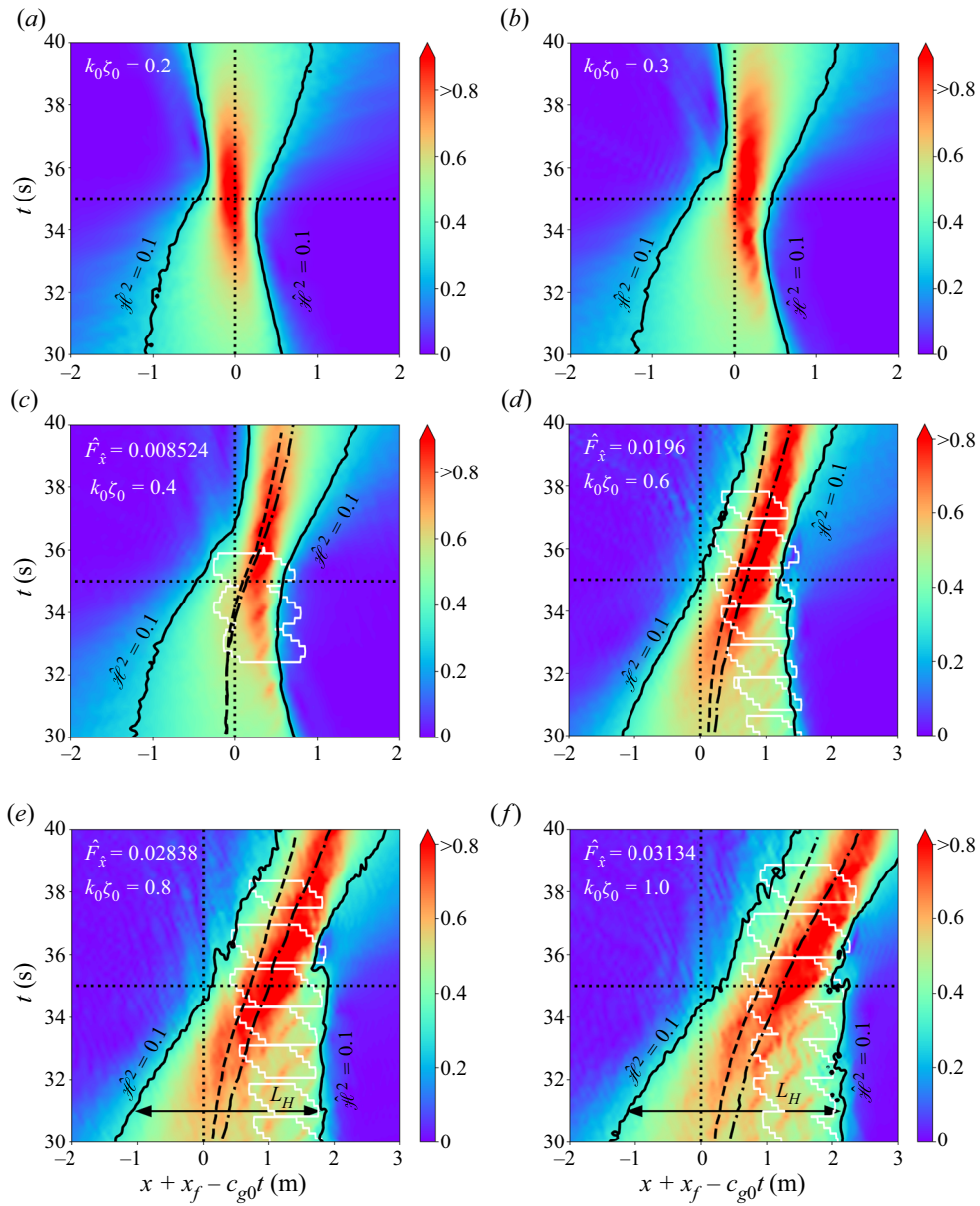


Figure 19. As in figure 18 for VOF model. Dashed and dash-dotted lines show $X_H(t)$ calculated from BEMv and VOF simulation results, respectively.

Significant increases in the propagation speed can be clearly seen for the breaking waves ($\hat{F}_{\hat{x}} > 0$), which may attain the following values: $v_{\text{BEMv}} \approx 1.27c_{g0}$ and $v_{\text{VOF}} \approx 1.36c_{g0}$. While the growth observed in BEMv computations is mostly related to the nonlinearities in the free-surface boundary conditions (2.2) and (2.3), the additional increment of speed present in the VOF model is likely caused by breaking-induced rotational flows.

It is known that the balance of spectral energy in wave forecasting models is closely dependent on wave group velocity, which is usually approximated by the linear dispersion relation (2.13). Stuhlmeier & Stiassnie (2019) pointed out that a more accurate nonlinear

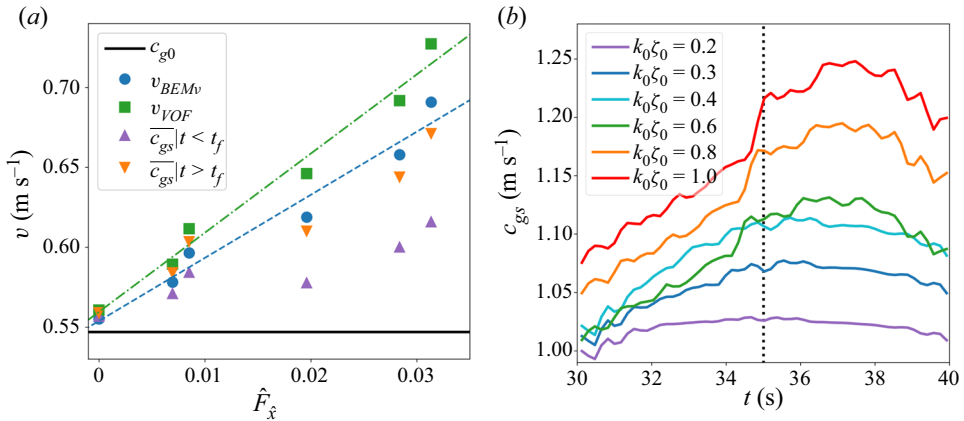


Figure 20. (a) Dependence of the wave train propagation velocity $v(t) = dX_H/dt$ on the energy dissipation rate \hat{F}_x (i.e. wave breaking strength). Dashed and dash-dotted lines represent the linear fit of the data derived from BEM v and VOF computations. Mean values of the spectral-weighted group velocities (4.4) obtained from the BEM v simulations are plotted for the wave train evolution before and after the linear focus ($t < t_f$ and $t > t_f$). (b) Variation of the spectral-weighted group velocities (4.4) with time obtained for the wave trains of different steepness $k_0 \zeta_0$ using the BEM v model.

approximation of group velocity derived from the Zakharov equation is needed. This means that the complex effect of wave breaking on group velocity is of practical importance and needs to be taken carefully into account.

Next, numerical results collected in the work are used to assess the validity of the spectral-weighted group velocity given by (4.4). The time series of c_{gs} calculated by the BEM v model for all the wave trains are depicted in figure 20(b). A gradual growth of c_{gs} is observed within the focusing stage for $t < t_f$ ($t_f = 35$ s) due to energy downshifting in the spectrum, see figure 12. It is interesting to see that the overall net change of c_{gs} becomes less pronounced after passing the linear focal point for each case. Since the spectra predicted by the BEM v and VOF models are close to each other, the values of c_{gs} calculated by these two models are similar to each other. Taking this into account, we estimate the mean values of c_{gs} for the focusing and defocusing stages separately, i.e. $\overline{c_{gs}}|_{t < t_f}$ and $\overline{c_{gs}}|_{t > t_f}$, see figure 20(a). As one can see, the estimates of $\overline{c_{gs}}$ for non-breaking and weakly breaking wave trains are close to the centroid velocity $v(t)$. A large increase in breaking strength can cause $\overline{c_{gs}}$ to deviate significantly from the centroid velocity in the focusing stage. Meanwhile $\overline{c_{gs}}$ is close to v_{BEMv} in the defocusing stage. Both estimates do not reflect the wave train propagation velocity computed by the VOF model as expected, since the derivation and calculation of c_{gs} are based on the linear assumption of all the wave components in the spectrum. Despite the deficiency of the spectral-weighted wave train propagation velocity, it can produce sufficiently accurate estimation of energy flux for numerical simulations or experimental measurements, see figure 9(b) and the expression (4.3). Note that we calculate energy fluxes for the VOF model with the expression (4.1) without introducing any simplifications.

Figure 21 exhibits the temporal evolution of wave group length L_H , which is defined as the distance between the leading and trailing edges of a wave train, as shown in figures 18 and 19. The wave group length is normalised by its value taken at $t = 30$ s when wave generation is completed in both BEM v and VOF models. As discussed above, all the non-breaking and weakly breaking wave trains ($0.2 \leq k_0 \zeta_0 \leq 0.4$) are subject to consequent focusing and defocusing stages due to dispersion. For strongly breaking waves

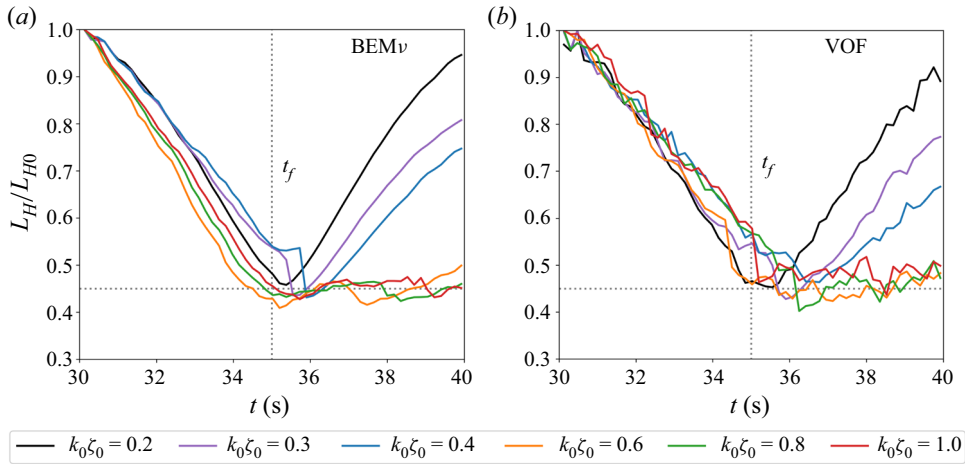


Figure 21. Evolution in time of the normalised length of the non-breaking to strongly breaking wave trains: (a) BEMv and (b) VOF computations. Definition of the wave train length is shown schematically in figures 18 and 19; L_{H0} is the initial wave train length.

with $k_0 \zeta_0 \geq 0.6$, the defocusing stage is suppressed, cf. figures 21(a) and 21(b). More importantly, the relative wave packet lengths after focusing are nearly constant and have similar magnitude in both BEMv and VOF computations: $L_H/L_{H0} = \text{const} \in [0.45, 0.5]$. Wave packet spreading is expected to resume after the breaking process is completed. However, the absolute values of wave group length computed by the BEMv and VOF models are different because of the wave evolution peculiarities during the focusing stage.

It has been reported that wind has a pronounced height amplification effect on broad-banded focusing wave groups in the defocusing stage (Touboul *et al.* 2008; Chambarel, Kharif & Kimmoun 2010). It is also of interest and importance to analyse the height amplification effect of wave breaking through the non-dimensional factor given by

$$\tilde{H}(t) = \frac{2 \times \max_x \{\mathcal{H}(x, t)\}}{H_S(k_0 \zeta_0 = 0.4)}. \quad (4.24)$$

Here, we introduce the normalisation by using the constant significant wave height H_S calculated for the wave train at the verge of stability, i.e. weakly breaking group with $k_0 \zeta_0 = 0.4$. Following the standard definition (Babanin *et al.* 2011), significant wave height can be calculated from (2.15)

$$H_S \equiv 4 \sqrt{\frac{1}{2\pi} \int_{-\infty}^{+\infty} \hat{\eta}^2(\omega) d\omega} = \sqrt[4]{\frac{8}{\pi}} \sqrt{m \zeta_0^2 T_0 (1 + \exp(-2\pi^2 m^2))}. \quad (4.25)$$

The factor of 2 is introduced into the numerator of (4.24) to evaluate the expected wave height from the envelope \mathcal{H} . Figure 22 shows the temporal evolution of wave height amplification factor defined by the expression (4.24). Linear regression is applied in panel (b) separately to the focusing ($t < 35$ s) and defocusing ($t > 35$ s) stages. It is clearly shown that the amplification of the non-breaking wave group ($k_0 \zeta_0 = 0.2$) is nearly symmetric about the focal point. An increase in the steepness parameter $k_0 \zeta_0$ causes certain asymmetry of \tilde{H} in the pre- and post-focusing stages, see (a).

It is usually expected that strong breaking leads to an instantaneous reduction of wave height. However, figure 22 demonstrates a quite opposite and non-trivial phenomenon.

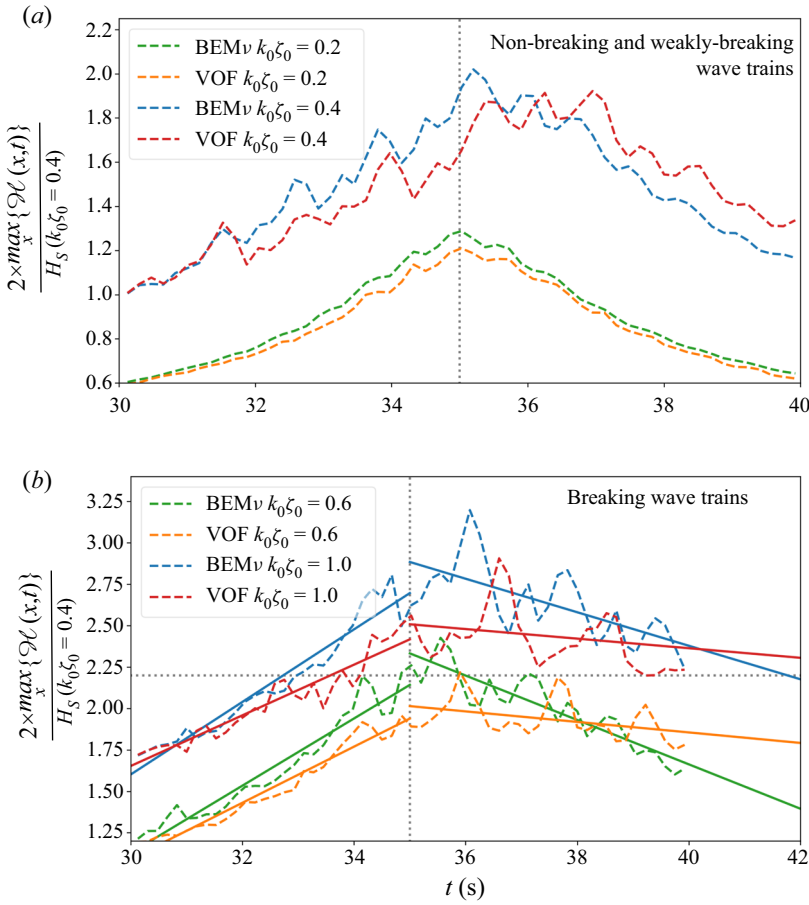


Figure 22. Evolution of the amplification factor \tilde{H} (4.24) observed in BEMv and VOF computations: (a) non- and weakly breaking wave trains, (b) strongly breaking wave trains. Dashed lines present the raw data derived from the computations, while solid lines are obtained by the linear interpolation of the plots separately at focusing and defocusing stages. Vertical dotted line shows focal point location at $t = 35$ s.

The height amplification factors of strongly breaking wave groups, in particular the solution for $k_0 \zeta_0 \geq 0.6$, decay much slower than the non-breaking and weakly breaking ones, cf. (a,b). This is probably due to the suppression of defocusing and the consequent conservation of wave train length shown in figure 21. Both VOF and BEMv models demonstrate asymmetry of \tilde{H} plots in the pre- and post-focusing stages with the increase of wave steepness especially when breaking is initiated. The wave train dynamics observed in the BEMv model is predominantly governed by the nonlinear wave interactions in the field, see discussion in § 4.4 and Appendix C. On the contrary, the wave train characteristic detected by the VOF model is appreciably different from the BEMv solution. This implies that important physical effects are not reflected in the quasi-potential approximation.

Under strong-breaking conditions, see (b), the peak values of \tilde{H} produced by the BEMv model are higher than the VOF calculations for each wave train. Unlike the BEMv model which shows significant decay rate of \tilde{H} in the post-focusing stage regardless of wave train steepness, the VOF solutions demonstrate a very mild decay of \tilde{H} over time for $k_0 \zeta_0 \geq 0.6$. The implication of this phenomenon is that the space (range of x) where extreme waves are

likely to appear might be larger in VOF simulations than FNP computations. For very steep wave trains $k_0\zeta_0 \geq 0.8$, their amplification factors remain above 2.2 for a relatively long time in the post-focusing stage as shown in figure 22(b). This can increase the occurrence probability and lifespan of extreme waves.

The change of wave dispersion as well as the conservation of height amplification factor recorded in our simulations are probably caused by breaking-induced rotational flows. These rotational motions are disregarded in the FNP model. According to Rapp & Melville (1990), the velocity field of breaking-induced flows consists of the contributions from the mean current, reflected and random waves, turbulence, etc. All of these contributions can be of significance as shown in figure 7. Decomposing the complex velocity field into various components mentioned above is not trivial but actually hardly feasible yet. To accomplish velocity decomposition, it requires substantial theoretical and numerical studies that are beyond the scope of the present work. Nevertheless, following the discussion of Longuet-Higgins (1992) it is probably reasonable to hypothesise that breaking-generated currents are dominant here. This is evident in the proposed empirical expression (4.19), which correlates the change of wave dispersion with the generation of rotational flows. Our calculations show that even a small value of $\tilde{U} \approx 5 \times 10^{-2} c_{g0}$ can cause a significant effect as shown in table 4 and figure 17. Therefore it is probably reasonable to infer that breaking waves interact with the induced currents in a two-way mechanism: breaking can produce currents, in turn the currents can influence the waves by suppressing the dispersion and maintaining the existence of steep waves for a longer time. An extensive theoretical study will be needed to carefully examine the hypothesis. The method of Shrira (1993) probably needs to be implemented for this task. To accomplish this task, a new method that can be used to decompose the velocity field should be developed. We would like to point out that the duration of a single breaking event, crucial for predictive oceanographic models (Kleiss & Melville 2010), is also an important topic requesting further attention.

5. Conclusions

A suite of low-fidelity (FNP) and coupled low-/high-fidelity (FNP–NS) flow models has been proposed to investigate the evolution of broad-banded wave trains under non-, moderate- and strong-breaking conditions. The weakly potential approximation proposed by Ruvinsky *et al.* (1991) was implemented in the FNP model to take into account the energy dissipation caused by wave breaking. This approximation was closed by the eddy viscosity model proposed by Tian *et al.* (2010, 2012).

The developed flow models were firstly tested with a narrow-banded wave train subject to modulational instability. Within the FNP model we also applied the free-surface re-meshing technique, which shows a similar performance as the eddy viscosity enclosure in the stabilisation of breaking wave simulation. The computed results were compared with laboratory measurements and other published calculations in terms of surface elevation. It was found that the high-fidelity results compare well with experiments. Although the low-fidelity calculations are rather close to the HOS solutions reported in the literature, they deviate from laboratory measurements especially at locations far away from the wavemaker.

To identify the underlying reason causing the deficiency of the eddy viscosity wave breaking model in the prediction of surface elevation, we further examined the FNP and FNP–NS models with six broad-banded focusing wave groups under non-, moderate- and strong-breaking conditions. A direct comparison of the low- and high-fidelity results reveals that the re-grid and eddy viscosity approaches predict accurately the energy

dissipation caused by breaking. We then applied spectral decomposition to compute the surface elevation of free waves by filtering out bound waves. Surprisingly, it was found that the amplitude spectra obtained from the FNP and NS solutions are practically identical in terms of magnitude, regardless of wavenumber and angular frequency. This led us to speculate that the underlying reason causing the deviation of FNP solutions from high-fidelity calculations (and laboratory measurements) in terms of surface elevation is the discrepancy in phase.

To verify this hypothesis, we undertook a detailed analysis of the phase difference between the FNP and NS results. It was found that the difference in phase grows with breaking intensity, and such an effect is especially profound for high-wavenumber components. We proposed an empirical formula to correlate the phase shift with wavenumber, energy dissipation rate and time in the power form by applying regression to the data. For strongly breaking wave trains it was found that the phase shift has a quadratic dependence on energy dissipation rate and wavenumber. Moreover, the shift of phase occurs at relatively high wavenumbers, but is hardly observed for long waves. It was also noticed that the growth of phase shift with time is nearly linear for strongly breaking waves. It is suggested that the observed variation in phases has similar physical origin as phase-locking effect reported by Derakhti & Kirby (2016). Therefore, phase locking is considered to be the main reason for inaccuracy of FNP predictions.

The proposed phase shift regression function was then used to study the dispersive property of breaking wave trains. It was found that weak breaking has very limited impact on the dispersion of fully nonlinear wave packets. On the contrary, strong breaking has great influence on the dispersive property of wave packets, causing the frequencies of high-wavenumber components to increase significantly. This phenomenon has been clearly demonstrated by using a 2-D Fourier transform of the high-resolution spatio-temporal records of surface elevation. We also showed that the dispersion variation can be derived from the phase shift regression function.

The change of wave dispersion caused by breaking increases the propagation speed of high-wavenumber components. In the NS computation of strongly breaking waves, the phase speeds of high-wavenumber components tend to be independent of the wavenumber i.e. these harmonics propagate at a similar speed. As a result, the dispersive spreading of wave train after the focal point is almost absent in all simulations of strongly breaking waves. It was found that the evolution of wave trains involving strong breaking consists of two distinctive stages: (i) a contraction of the wave train length and an accompanying growth of the wave height due to focusing; and (ii) maintaining a nearly constant wave train length after the focal point instead of spreading out immediately as usually expected. This unusual conservation of wave train length is of significance because it can prolong the lifespan of focused waves and expand the space for their propagation. This can raise the probability of extreme wave formation in breaking scenarios compared with non-breaking environments. Such an unexpected finding is contradictory to our general impression that strong breaking can instantaneously reduce wave height by destructing initially stable harmonics and dissipating their mechanical energy.

The proposed empirical expression (4.19) correlates the change of wave dispersion with the breaking-induced rotational flow captured in our high-fidelity simulations. The oceanography community recommends investigating wave-induced currents as a priority in the research of wind-wave problems (Greenslade *et al.* 2020). For wind speeds larger than 7.5 m s^{-1} , most of the wind stress goes to generating wind waves rather than surface currents (Greenslade *et al.* 2020). Under these conditions, wave breaking is considered as an important source for generating currents (Greenslade *et al.* 2020). A detailed theoretical

study is needed to examine the evolution of breaking waves coupled with breaking-induced currents. Such a study can build on the time-varying non-potential velocity fields, which need to be extracted from the VOF simulations. The extracted information can then be used as the input for the theoretical analysis proposed by Shrira (1993).

We would like to emphasise that in the current stage the conclusions drawn here are based on, and possibly limited to, the quantitative analysis of the wave trains considered in the present work. More comprehensive theoretical, numerical and experimental investigations are needed to arrive at definitive conclusions on phase shifting and other related phenomena reported in this paper. The outcomes of the current research can be beneficial to the development of more accurate theoretical models for wave breaking, which can be used in the weakly and fully nonlinear modelling of ocean waves for engineering and environmental science.

Acknowledgements. We would like to express our deep appreciation to Professor Ling Qian and Dr Wei Bai from Manchester Metropolitan University, UK for advising and supporting this research, and to Professor Lev Shemer from Tel Aviv University, Israel for his encouragement and constructive advice helping us to improve the quality of the manuscript. We also thank two anonymous reviewers for their incisive comments and valuable advice.

Funding. This work was supported by the Engineering and Physical Sciences Research Council (EPSRC), U.K. Project: High-fidelity Simulation of Air Entrainment in Breaking Wave Impacts, under Grant No. EP/S011862/1.

Declaration of interests. The authors report no conflict of interest.

Author ORCIDs.

 Anatoliy Khait <https://orcid.org/0000-0003-2453-9898>;

 Zhihua Ma <https://orcid.org/0000-0002-2426-3038>.

Appendix A. Grid convergence

The grid convergence of BEM_v and VOF numerical models is studied with respect to the modulated wave train (2.12). The grid density determined as number of cells (nodes) distributed along the carrier wave length λ_0 is used for characterisation of the grid quality. This allows generalisation of the convergence study outcomes to other wave trains investigated in the paper. Four grids of different free surface mesh density ranging from 16 to 32 cells per λ_0 are considered in the BEM_v model, see figure 23. All meshes show identical surface elevation plots close to the wavemaker ($x = 35$ m), as well as far away from it ($x = 50$ m). Nevertheless, the finest mesh is used in the present work.

The grid resolutions of 64 to 256 cells per carrier wavelength λ_0 were considered in convergence study of the VOF model, see figure 24. In this case, first two grids fail in simulation of the waves dispersion. The grid densities 192 and 256 cells per λ_0 showed practically identical results at $x = 35$ m. Deviation between the results obtained with these two grids at $x = 50$ m is acceptably small, thus the convergence is established with respect to the free-surface elevation. The finest grid of density 256 cells per λ_0 is used for the computations.

Appendix B. Coefficients of the weakly nonlinear Zakharov model

Assume $A(k)$ being the discrete complex wavenumber spectrum of the free waves only. Introduce the following wavenumbers:

$$k_b = k_m + k_n \quad \text{and} \quad k_c = -k_m + k_n \quad \text{and} \quad k_d = -k_m - k_n. \quad (\text{B1a-c})$$

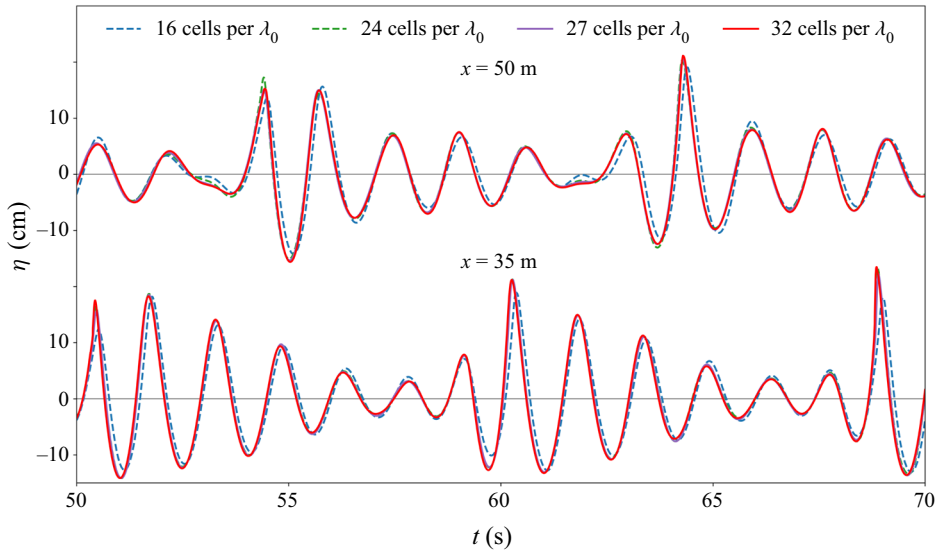


Figure 23. Surface elevation obtained in BEMv computations at two coordinates measured from the wavemaker location: $x = 35$ and $x = 50$ m.

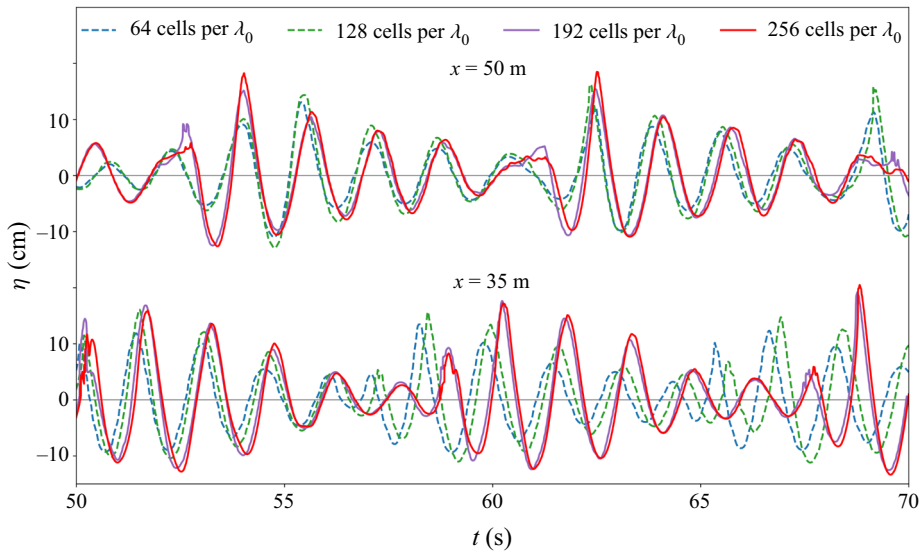


Figure 24. As in figure 23 for the results of VOF computations.

The corresponding angular frequencies due to dispersion relation (2.13) are

$$\omega_b = \sqrt{gk_b \tanh(k_b h)} \quad \text{and} \quad \omega_c = \sqrt{gk_c \tanh(k_c h)} \quad \text{and} \quad \omega_d = \sqrt{gk_d \tanh(k_d h)}. \quad (\text{B2a-c})$$

The complex wavenumber amplitudes in the 2nd-order bound waves spectrum required to complete expression (2.20) are (Stiassnie & Shemer 1987; Krasitskii 1994)

$$B(k_m, k_n) = -\pi \sqrt{\frac{2g\omega_b}{\omega_m \omega_n}} \frac{V(\omega_b, \omega_m, \omega_n, k_m + k_n, k_m, k_n)}{\omega_b - \omega_m - \omega_n} A_m A_n \quad (\text{B3})$$

$$C(k_m, k_n) = -\pi \sqrt{\frac{2g\omega_c}{\omega_m\omega_n}} \frac{W(\omega_c, \omega_m, \omega_n, -k_m + k_n, k_m, k_n)}{\omega_c + \omega_m - \omega_n} A_m^* A_n \quad (\text{B4})$$

$$D(k_m, k_n) = -\pi \sqrt{\frac{2g\omega_d}{\omega_m\omega_n}} \frac{T(\omega_d, \omega_m, \omega_n, -k_m - k_n, k_m, k_n)}{\omega_d + \omega_m + \omega_n} A_m^* A_n^*. \quad (\text{B5})$$

Here, m and n are numbers of harmonics in the discrete free waves complex spectrum $A(k)$; the star superscript ‘*’ stands for the complex conjugation. The expressions for the coefficients V , W and T are (Stiassnie & Shemer 1987)

$$V(\omega_0, \omega_1, \omega_2, k_0, k_1, k_2) = \frac{1}{4\pi} \sqrt{\frac{g}{2}} \left\{ \frac{1}{2} \sqrt{\frac{\omega_0}{\omega_1\omega_2}} \left[\left(\frac{\omega_1\omega_2}{g} \right)^2 + k_1k_2 \right] - \sqrt{\frac{\omega_2}{\omega_0\omega_1}} \left[\left(\frac{\omega_0\omega_1}{g} \right)^2 - k_0k_1 \right] \right\} \quad (\text{B6})$$

$$W(\omega_0, \omega_1, \omega_2, k_0, k_1, k_2) = \frac{1}{4\pi} \sqrt{\frac{g}{2}} \left\{ \sqrt{\frac{\omega_2}{\omega_0\omega_1}} \left[\left(\frac{\omega_0\omega_1}{g} \right)^2 + k_0k_1 \right] - \sqrt{\frac{\omega_1}{\omega_0\omega_2}} \left[\left(\frac{\omega_0\omega_2}{g} \right)^2 - k_0k_2 \right] - \sqrt{\frac{\omega_0}{\omega_1\omega_2}} \left[\left(\frac{\omega_1\omega_2}{g} \right)^2 - k_1k_2 \right] \right\} \quad (\text{B7})$$

$$T(\omega_0, \omega_1, \omega_2, k_0, k_1, k_2) = \frac{1}{4\pi} \sqrt{\frac{g}{2}} \left\{ \sqrt{\frac{\omega_2}{\omega_0\omega_1}} \left[\left(\frac{\omega_0\omega_1}{g} \right)^2 + k_0k_1 \right] + \frac{1}{2} \sqrt{\frac{\omega_0}{\omega_1\omega_2}} \left[\left(\frac{\omega_1\omega_2}{g} \right)^2 + k_1k_2 \right] \right\}. \quad (\text{B8})$$

Appendix C. Eddy viscosity damping in the framework of the modified nonlinear Schrödinger equation

The variation of wave train dispersion is reported in the current study for the quasi-potential solutions of the BEM ν model, which is closed with the eddy viscosity wave breaking approximation (EVBM). It is interesting and important to identify the main source of the observed effects in waves dispersion: whether they are caused by the fully nonlinear wave interactions or augmented by the applied empirical EVBM. For simplicity we consider the evolution of a weakly nonlinear wave train in the framework of the modified nonlinear Schrödinger equation (MNLSE).

Our numerical experiments with the BEM ν model show that, within the adopted eddy viscosity breaking closure, the viscous term in the kinematic boundary condition (2.2) has negligible effect as compared with that in the dynamic boundary condition (2.3). Therefore, a simplification of (2.2) introduced by Tian *et al.* (2010) is permitted. Substitution of the linearised kinematic boundary condition to (2.4) allows its integration with time. Substitution of the obtained form of $\partial\psi/\partial s$ into (2.2) leads to simplified

kinematic and dynamic boundary conditions

$$\frac{\partial \eta}{\partial t} = \frac{\partial \eta}{\partial x} \frac{\partial \varphi}{\partial x} - \frac{\partial \varphi}{\partial z} - 2\nu_{eddy} \frac{\partial^2 \eta}{\partial x^2}, \quad (C1)$$

$$\frac{\partial \varphi}{\partial t} = g\eta - \frac{1}{2}|\nabla \varphi|^2 + 2\nu_{eddy} \frac{\partial^2 \varphi}{\partial x^2}, \quad (C2)$$

where η is surface elevation. Starting with the water waves problem given by the boundary conditions above and assuming the deep-water limit, Dias *et al.* (2008) derived a weakly damped form of the nonlinear Schrödinger equation (NLSE), which can be extended to MNLSE

$$\underbrace{\frac{\partial A}{\partial \xi} + i \frac{\partial^2 A}{\partial \tau^2}}_{\text{I (LSE)}} + \underbrace{i|A|^2 A}_{\text{II (NLSE)}} + \underbrace{8\varepsilon|A|^2 \frac{\partial A}{\partial \tau} + 2\varepsilon A^2 \frac{\partial A^*}{\partial \tau} + 4i\varepsilon A \frac{\partial \Phi}{\partial \tau}}_{\text{III (MNLSE)}} \bigg|_{Z=0} + \underbrace{2\nu_{eddy} \frac{k_0^2}{\omega_0} A}_{\text{IV (damping)}} = 0. \quad (C3)$$

Asterisk * designates complex conjugation, LSE stands for the linear Schrödinger equation. The dimensionless potential Φ is governed by the following equations:

$$4 \frac{\partial^2 \Phi}{\partial \tau^2} + \frac{\partial^2 \Phi}{\partial Z^2} = 0 \quad Z < 0 \quad (C4)$$

$$\frac{\partial \Phi}{\partial Z} = \frac{\partial |A|^2}{\partial \tau} \quad Z = 0 \quad (C5)$$

$$\frac{\partial \Phi}{\partial Z} = 0 \quad Z \rightarrow -\infty. \quad (C6)$$

Surface elevation is given by the dimensionless complex envelope A in the following way: $\eta = \zeta_0 \text{Re}\{A \exp(i(k_0 x - \omega_0 t))\}$, where ζ_0 , k_0 , and ω_0 are carrier wave amplitude, wavenumber and angular frequency, respectively. The dimensionless variables are defined as

$$\tau = \varepsilon \omega_0 \left(\frac{x}{c_g} - t \right) \quad \xi = \varepsilon^2 k_0 x \quad \varphi = \omega_0 \zeta_0^2 \Phi \quad Z = \varepsilon k_0 z. \quad (C7a-d)$$

To satisfy the narrow-band restriction implied by (C3), we select the parameter $m = 4$ in (2.14). A steep wave train of $\varepsilon = 0.24$ is considered. The eddy viscosity is assumed to be of an order $\nu_{eddy} = O(10^{-3}) \text{ m}^2 \text{ s}^{-1}$. Other parameters of the wave train (2.14) are similar to the main part of the paper. The initial shape of the wave train is shown in figure 25(a). Equation (C3) was solved numerically by using the pseudo-spectral method of Lo & Mei (1985) to find the wave train shape at the linear focus $x = x_f = 8.5 \text{ m}$, as shown in (b). Here, we pay close attention to the influence of different terms in (C3) (designated by I, II, III and IV) on the nonlinear evolution of the wave train. The solution to the linear part of (C3), i.e. LSE, suggests mild shortening of the wave train envelope due to dispersive focusing. The envelope shape for the NLSE demonstrates significant enhancement of the wave height at the linear focus, while the wave train propagation speed seems to be similar to the linear evolution case. Including the higher-order terms and then solving MNLSE, we can see more complicated behaviours with a significant speed-up of the wave train propagation. Note that the obtained wave train shapes are in a good agreement with experiments of Shemer, Kit & Jiao (2002), and the nonlinear speed-up

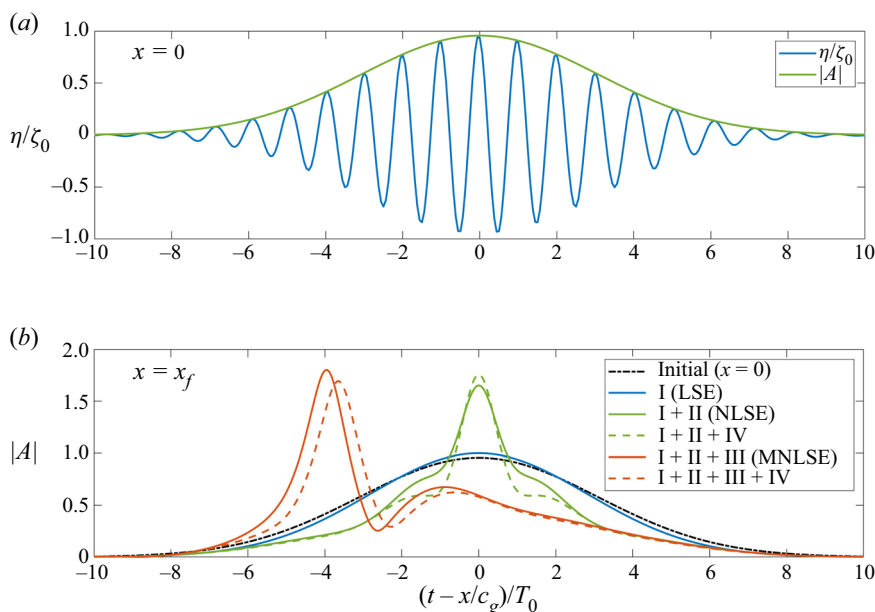


Figure 25. Evolution of the wave train governed by the equation (C3) with an emphasis on the impact of different terms: (a) initial shape of the wave train at $x = 0$; (b) wave train shape at the linear focus $x = x_f = 8.5$ m.

is a well-documented phenomenon (Chereskin & Mollo-Christensen 1985; Trulsen 1998; Pizzo & Melville 2016).

The main concern now is the effect of the damping term IV in (C3). As one can see, adding this term to NLSE, i.e. case I + II + IV, does not cause any variation of the wave train propagation speed. Interestingly, the viscous damping resulted in a mild increase of the wave height at the focusing location and appreciable reduction elsewhere. Moreover, introducing the term IV to the full version of MNLSE does not lead to any increase in the wave train propagation speed. On the contrary, it results in a moderate deceleration due to gradual energy dissipation. Based on the given observations we can conclude that the wave train speed-up observed in BEM ν calculations is more likely a result of the nonlinear wave component interactions than an outcome of the eddy viscosity breaking closure (EVBm). Note that the variation of v_{eddy} in space and time ignored in MNLSE is not likely to play a role in the acceleration of wave trains. It implies that a recalibration of EVBM probably will not improve the computation accuracy to the same level of the high-fidelity NS simulation. The underlying reason is perhaps due to the important interactions of the wave train with the breaking-generated rotational flows ignored by EVBM. It could be valuable to study the impact of breaking-generated sheared currents on the propagation of carrier wave train.

REFERENCES

- ANNENKOV, S.Y. & SHRIRA, V.I. 2018 Spectral evolution of weakly nonlinear random waves: kinetic description versus direct numerical simulations. *J. Fluid Mech.* **844**, 766–795.
- BABANIN, A.V. 2011 *Breaking and Dissipation of Ocean Surface Waves*. Cambridge University Press.
- BABANIN, A.V. & CHALIKOV, D. 2012 Numerical investigation of turbulence generation in non-breaking potential waves. *J. Geophys. Res.* **117**, C06010.

- BABANIN, A.V., WASEDA, T., KINOSHITA, T. & TOFFOLI, A. 2011 Wave breaking in directional fields. *J. Phys. Oceanogr.* **41**, 145–156.
- BANNER, M.L., BARTHELEMY, X., FEDELE, F., ALLIS, M., BENETAZZO, A., DIAS, F. & PEIRSON, W.L. 2014 Linking reduced breaking crest speeds to unsteady nonlinear water wave group behavior. *Phys. Rev. Lett.* **112**, 114502.
- BANNER, M.L. & PEIRSON, W.L. 2007 Wave breaking onset and strength for two-dimensional deep-water wave groups. *J. Fluid Mech.* **585**, 93–115.
- BULLOCK, G.N., OBHRAI, C., PEREGRINE, D.H. & BREDMOSE, H. 2007 Violent breaking wave impacts. Part 1: results from large-scale regular wave tests on vertical and sloping walls. *Coast. Engng* **54** (8), 602–617.
- CHALIKOV, D. & BABANIN, A.V. 2014 Simulation of one-dimensional evolution of wind waves in a deep water. *Phys. Fluids* **26**, 096607.
- CHALIKOV, D. & SHEININ, D. 2005 Modeling extreme waves based on equations of potential flow with a free surface. *J. Comput. Phys.* **210**, 247–273.
- CHAMBAREL, J., KHARIF, C. & KIMMOUN, O. 2010 Generation of two-dimensional steep water waves on finite depth with and without wind. *Eur. J. Mech. B/Fluids* **29**, 132–142.
- CHERESKIN, T.K. & MOLLO-CHRISTENSEN, E. 1985 Modulational development of nonlinear gravity-wave groups. *J. Fluid Mech.* **151**, 337–365.
- CRACIUNESCU, C.C. & CHRISTOU, M. 2020 Wave breaking energy dissipation in long-crested focused wave groups based on jonswap spectra. *Appl. Ocean Res.* **99**, 102144.
- DE VITA, F., VERZICCO, R. & IAFRATI, A. 2018 Breaking of modulated wave groups: kinematics and energy dissipation processes. *J. Fluid Mech.* **855**, 267–298.
- DEAN, R.G. & DALRYMPLE, R.A. 1991 *Water Wave Mechanics for Engineers and Scientists*. World Scientific.
- DEIKE, L., MELVILLE, W. & POPINET, S. 2016 Air entrainment and bubble statistics in breaking waves. *J. Fluid Mech.* **801**, 91–129.
- DEIKE, L., PIZZO, N. & MELVILLE, W.K. 2017 Lagrangian transport by breaking surface waves. *J. Fluid Mech.* **829**, 364–391.
- DEIKE, L., POPINET, S. & MELVILLE, W. 2015 Capillary effects on wave breaking. *J. Fluid Mech.* **769**, 541–569.
- DERAKHTI, M. & KIRBY, J.T. 2016 Breaking-onset, energy and momentum flux in unsteady focused wave packets. *J. Fluid Mech.* **790**, 553–581.
- DIAS, F., DYACHENKO, A.I. & ZAKHAROV, V.E. 2008 Theory of weakly damped free-surface flows: a new formulation based on potential flow solutions. *Phys. Lett. A* **372** (8), 1297–1302.
- DOSAEV, A., TROITSKAYA, Y.I. & SHRIRA, V.I. 2021 On the physical mechanism of front-back asymmetry of non-breaking gravity-capillary waves. *J. Fluid Mech.* **906**, A11.
- DRAZEN, D.A., MELVILLE, W.K. & LENAIN, L. 2008 Inertial scaling of dissipation in unsteady breaking waves. *J. Fluid Mech.* **611**, 307–332.
- DUCROZET, G., BONNEFOY, F., LE TOUZÉ, D. & FERRANT, P. 2012 A modified high-order spectral method for wavemaker modeling in a numerical wave tank. *Eur. J. Mech. B/Fluids* **34**, 19–34.
- DUCROZET, G., BONNEFOY, F., LE TOUZÉ, D. & FERRANT, P. 2016 Hos-ocean: open-source solver for nonlinear waves in open ocean based on high-order spectral method. *Comput. Phys. Commun.* **203**, 245–254.
- DUNCAN, J.H. 1983 The breaking and non-breaking wave resistance of a two-dimensional hydrofoil. *J. Fluid Mech.* **126**, 507–520.
- FEDELE, F., BANNER, M.L. & BARTHELEMY, X. 2020 Crest speeds of unsteady surface water waves. *J. Fluid Mech.* **899**, A5.
- FEDELE, F., CHANDRE, C. & FARAZMAND, M. 2016 Kinematics of fluid particles on the sea surface: Hamiltonian theory. *J. Fluid Mech.* **801**, 260–288.
- GIBSON, R.S. & SWAN, C. 2006 The evolution of large ocean waves: the role of local and rapid spectral changes. *Proc. R. Soc. A* **463**, 21–48.
- GREENSLADE, D., *et al.* 2020 15 priorities for wind-waves research: an Australian perspective. *Bull. Am. Meteorol. Soc.* **101**, E446–E461.
- GRILLI, S.T., SKOURUP, J. & SVENDSEN, I.A. 1989 An efficient boundary element method for nonlinear water waves. *Engng Anal. Bound. Elem.* **6** (2), 97–107.
- GRILLI, S.T. & SUBRAMANYA, R. 1996 Numerical modeling of wave breaking induced by fixed or moving boundaries. *Comput. Mech.* **17**, 374–391.
- GRILLI, S.T. & SVENDSEN, I.A. 1990 Corner problems and global accuracy in the boundary element solution of nonlinear wave flows. *Engng Anal. Bound. Elem.* **7**, 178–195.

- HASAN, S.A., SRIRAM, V. & SELVAM, R.P. 2019 Evaluation of an eddy viscosity type wave breaking model for intermediate water depths. *Eur. J. Mech. B/Fluids* **78**, 115–138.
- HOUTANI, H., WASEDA, T., FUJIMOTO, W., KIYOMATSU, K. & TANIZAWA, K. 2018a Generation of a spatially periodic directional wave field in a rectangular wave basin based on higher-order spectral simulation. *Ocean Engng* **169**, 428–441.
- HOUTANI, H., WASEDA, T. & TANIZAWA, K. 2018b Experimental and numerical investigations of temporally and spatially periodic modulated wave trains. *Phys. Fluids* **30**, 034101.
- HU, Z.Z., MAI, T., GREAVES, D. & RABY, A. 2017 Investigations of offshore breaking wave impacts on a large offshore structure. *J. Fluids Struct.* **75**, 99–116.
- IAFRATI, A. 2009 Numerical study of the effects of the breaking intensity on wave breaking flows. *J. Fluid Mech.* **622**, 371–411.
- IAFRATI, A., BABANIN, A. & ONORATO, M. 2013 Modulational instability, wave breaking, and formation of large-scale dipoles in the atmosphere. *Phys. Rev. Lett.* **110**, 184504.
- IAFRATI, A., DE VITA, F. & VERZICCO, R. 2019 Effects of the wind on the breaking of modulated wave trains. *Eur. J. Mech. B/Fluids* **73**, 6–23.
- KAPSENBERG, G.K. 2011 Slamming of ships: where are we now? *Phil. Trans. R. Soc. A* **369** (1947), 2892–2919.
- KHAIT, A. & SHEMER, L. 2018 On the kinematic criterion for the inception of breaking in surface gravity waves: fully nonlinear numerical simulations and experimental verification. *Phys. Fluids* **30**, 057103.
- KHAIT, A. & SHEMER, L. 2019a Application of boundary element method for determination of the wavemaker driving signal. *J. Offshore Mech. Arctic Engng* **141**, 061102.
- KHAIT, A. & SHEMER, L. 2019b Nonlinear wave generation by a wavemaker in deep to intermediate water depth. *Ocean Engng* **182**, 222–234.
- KIGER, K.T. & DUNCAN, J.H. 2012 Air-entrainment mechanisms in plunging jets and breaking waves. *Annu. Rev. Fluid Mech.* **44**, 563–596.
- KLEISS, J.M. & MELVILLE, W.K. 2010 Observations of wave breaking kinematics in fetch-limited seas. *J. Phys. Oceanogr.* **40**, 2575–2604.
- KRASITSKII, V.P. 1994 On the reduced equations in the hamiltonian theory of weakly nonlinear surface waves. *J. Fluid Mech.* **272**, 1–20.
- KROGSTAD, H.E. & TRULSEN, K. 2010 Interpretations and observations of ocean wave spectra. *Ocean Dyn.* **60**, 973–991.
- LARSEN, B.E., FUHRMAN, D.R. & ROENBY, J. 2019 Performance of interfoam on the simulation of progressive waves. *Coast. Engng J.* **61** (3), 380–400.
- LENAIN, L., PIZZO, N. & MELVILLE, W.K. 2019 Laboratory studies of lagrangian transport by breaking surface waves. *J. Fluid Mech.* **876**, R1.
- LO, E. & MEI, C.C. 1985 A numerical study of water-wave modulation based on a higher-order nonlinear Schrödinger equation. *J. Fluid Mech.* **150**, 395–416.
- LONGUET-HIGGINS, M.S. 1992 Theory of weakly damped stokes waves: a new formulation and its physical interpretation. *J. Fluid Mech.* **235**, 319–324.
- LUBIN, P. & GLOCKNER, S. 2015 Numerical simulations of three-dimensional plunging breaking waves: generation and evolution of aerated vortex filaments. *J. Fluid Mech.* **767**, 364–393.
- MA, Z.H., CAUSON, D.M., QIAN, L., MINGHAM, C.G., GU, H.B. & MARTÍNEZ FERRER, P. 2014 A compressible multiphase flow model for violent aerated wave impact problems. *Proc. R. Soc. A* **470**, 20140542.
- MA, Z.H., CAUSON, D.M., QIAN, L., MINGHAM, C.G. & MARTÍNEZ FERRER, P. 2016 Numerical investigation of air enclosed wave impacts in a depressurised tank. *Ocean Engng* **123**, 15–27.
- MARTÍNEZ FERRER, P.J., CAUSON, D.M., QIAN, L., MINGHAM, C.G. & MA, Z.H. 2016 A multi-region coupling scheme for compressible and incompressible flow solvers for two-phase flow in a numerical wave tank. *Comput. Fluids* **125**, 116–129.
- MELVILLE, W.K. 1983 Wave modulation and breakdown. *J. Fluid Mech.* **128**, 489–506.
- MELVILLE, W.K. 1994 Energy dissipation by breaking waves. *J. Phys. Oceanogr.* **24**, 2041–2049.
- MELVILLE, W.K. 1996 The role of surface-wave breaking in air-sea interaction. *Annu. Rev. Fluid Mech.* **28** (1), 279–321.
- OLIVEIRA, P.J. & ISSA, R.I. 2001 An improved PISO algorithm for the computation of buoyancy-driven flows. *Numer. Heat Transfer B* **40**, 473–493.
- PERLIN, M., CHOI, W. & TIAN, Z. 2013 Breaking waves in deep and intermediate waters. *Annu. Rev. Fluid Mech.* **45**, 115–145.
- PIZZO, N.E. & MELVILLE, W.K. 2016 Wave modulation: the geometry, kinematics, and dynamics of surface-wave packets. *J. Fluid Mech.* **803**, 292–312.

- RAMAMONJIARISOA, A. & MOLLO-CHRISTENSEN, E. 1979 Modulation characteristics of sea surface waves. *J. Geophys. Res.* **84** (C12), 7769–7775.
- RAPP, R.J. & MELVILLE, W.K. 1990 Laboratory measurements of deep-water breaking waves. *Phil. Trans. R. Soc. Lond. A* **331**, 735–800.
- ROMERO, L., MELVILLE, W.K. & KLEISS, J.M. 2012 Spectral energy dissipation due to surface wave breaking. *J. Phys. Oceanogr.* **42**, 1421–1444.
- RUVINSKY, K.D., FELDSTEIN, F.I. & FREIDMAN, G.I. 1991 Numerical simulations of the quasi-stationary stage of ripple excitation by steep gravity–capillary waves. *J. Fluid Mech.* **230**, 339–353.
- SEIFFERT, B.R. & DUCROZET, G. 2018 Simulation of breaking waves using the high-order spectral method with laboratory experiments: wave-breaking energy dissipation. *Ocean Dyn.* **68**, 65–89.
- SEIFFERT, B.R., DUCROZET, G. & BONNEFOY, F. 2017 Simulation of breaking waves using the high-order spectral method with laboratory experiments: wave-breaking onset. *Ocean Model.* **119**, 94–104.
- SHEMER, L., GOULITSKI, K. & KIT, E. 2007 Evolution of wide-spectrum unidirectional wave groups in a tank: an experimental and numerical study. *Eur. J. Mech. B/Fluids* **26**, 193–219.
- SHEMER, L., KIT, E. & JIAO, H. 2002 An experimental and numerical study of the spatial evolution of unidirectional nonlinear water-wave groups. *Phys. Fluids* **14**, 3380.
- SHRIRA, V.I. 1993 Surface waves on shear currents: solution of the boundary-value problem. *J. Fluid Mech.* **252**, 565–584.
- STANSELL, P. & MACFARLANE, C. 2002 Experimental investigation of wave breaking criteria based on wave phase speeds. *J. Phys. Oceanogr.* **32**, 1269–1283.
- STIASSNIE, M. & SHEMER, L. 1984 On modification of Zakharov equation for surface gravity waves. *J. Fluid Mech.* **143**, 47–67.
- STIASSNIE, M. & SHEMER, L. 1987 Energy computations for evolution of class i and ii instabilities of Stokes waves. *J. Fluid Mech.* **174**, 299–312.
- STUHLMEIER, R. & STIASSNIE, M. 2019 Nonlinear dispersion for ocean surface waves. *J. Fluid Mech.* **859**, 49–58.
- SUBRAMANYA, R. & GRILLI, S.T. 1994 Domain regridding in the computation of nonlinear waves. *Trans. Model. Simul.* **9**, 139–150.
- TIAN, Z., PERLIN, M. & CHOI, W. 2008 Evaluation of a deep-water wave breaking criterion. *Phys. Fluids* **20**, 066604.
- TIAN, Z., PERLIN, M. & CHOI, W. 2010 Energy dissipation in two-dimensional unsteady plunging breakers and an eddy viscosity model. *J. Fluid Mech.* **655**, 217–257.
- TIAN, Z., PERLIN, M. & CHOI, W. 2012 An eddy viscosity model for two-dimensional breaking waves and its validation with laboratory experiments. *Phys. Fluids* **24**, 036601.
- TOUBOUL, J., KHARIF, C., PELINOVSKY, E. & GIOVANANGELI, J.-P. 2008 On the interaction of wind and steep gravity wave groups using miles’ and Jeffreys’ mechanisms. *Nonlinear Process. Geophys.* **15**, 1023–1031.
- TRULSEN, K. 1998 Crest pairing predicted by modulation theory. *J. Geophys. Res.* **103** (C2), 3143–3147.
- VERON, F. 2015 Ocean spray. *Annu. Rev. Fluid Mech.* **47**, 507–538.
- WHITHAM, G.B. 1999 *Linear and Nonlinear Waves*. John Wiley & Sons.
- ZAKHAROV, V.E. 1968 Stability of periodic waves of finite amplitude on the surface of a deep fluid. *J. Appl. Mech. Tech. Phys.* **9**, 190–194.